Ore Geology Reviews 150 (2022) 105146

Contents lists available at ScienceDirect

Ore Geology Reviews

journal homepage: www.elsevier.com/locate/oregeorev

Sources of rare earth elements and yttrium in the early Cambrian phosphorites in Zhijin, southwest China

Shengwei Wu [a,b], Haifeng Fan [a,b,*], Yong Xia [a,b], Qingtian Meng [c], Xingxiang Gong [d], Shan He [a,b], Xiqiang Liu [a], Haiying Yang [e], Hanjie Wen [b,f]

[a] State Key Laboratory of Ore Deposit Geochemistry, Institute of Geochemistry, Chinese Academy of Sciences, Guiyang 550081, China
[b] University of Chinese Academy of Sciences, Beijing 100049, China
[c] No. 104 Geological Team, Guizhou Bureau of Geology and Mineral Exploration & Development, Guiyang 550081, China
[d] Reserve Bureau of Land and Mineral Resources of Guizhou Province, Guiyang 550081, China
[e] School of Earth Sciences, Yunnan University, Kunming 650500, China
[f] School of Earth Sciences and Resources, Chang'an University, Xi'an 710054, China

ARTICLE INFO

Keywords:
REY sources
Early Cambrian
Phosphorites
Granite weathering

ABSTRACT

The early Cambrian Zhijin phosphorite in Guizhou province, China, has high rare earth elements and yttrium (REY) contents of up to 2500 ppm, with heavy REY (HREY) accounting for ~30 % of the total REY. However, their REY sources are not well-determined. Herein, elemental geochemistry and Sr–Nd isotopes of phosphorites in four sections from the Zhijin phosphorite ore area were investigated, primarily to constrain the contributions of seawater and terrestrial REY sources to the REY enrichment in these phosphorites. Zhijin phosphorites have high Y/Ho (45–63) and seawater signature's $^{87}Sr/^{86}Sr(i)$ ratios (0.7085–0.7092), suggesting a partial contribution from seawater-sourced REY. On the other hand, Zhijin phosphorites have $\varepsilon_{Nd}(t)$ values of −8.6 – −6.8, indicative of the great influence from continental weathering. The Y/Ho ratios exhibit negative correlations with their Zr contents and Sm_N/Yb_N ratios; meanwhile the $^{87}Sr/^{86}Sr(i)$ ratios exhibit positive correlations with their Sr contents and REY contents, indicating that terrestrial source contributions played an important role in REY enrichment in Zhijin phosphorites. Furthermore, the provenance of Zhijin shales indicates the terrigenous granite weathering, during which the regolith-hosted REY could be transported to Zhijin shallow seawater, providing abundant REY to Zhijin phosphorites. We proposed that the REY enrichment in Zhijin phosphorites could be associated with high REY seawater induced by granite weathering. This study provides a new perspective on the relationship between granite weathering and marine REY deposition, which may be a common phenomenon in geological history but remains to be fully investigated in future.

1. Introduction

Rare earth elements and yttrium (REY) have been widely used in energy, electronic information industry, and the national defense security (Humphries, 2012). They can be separated into light REY (LREY, La-Nd), middle REY (MREY, Sm-Ho), and heavy REY (HREY, Er-Lu and Y). The current relatively scarce HREY mainly originates from ion adsorption-type REY deposits in South China, which dominates the market because of their low mining and metallurgical costs (Kynicky et al., 2012; Long et al., 2012). It has been suggested that the REY associated with marine sedimentary phosphorite ore deposits also exhibits potential economic value, especially the HREY, which might mitigate the global REY crisis (Emsbo et al., 2015). For example, pure francolite from the Miocene Hawthorn Formation in the United States contains a median REY concentration of 900 ppm, wherein 400 ppm is the total HREY concentration (Emsbo et al., 2015). In South China, there are many phosphorite ore deposits, among which the Zhijin phosphorite ore deposit in Guizhou province shows extreme REY enrichment. The average REY content of francolite grains in this deposit is ~2250 ppm, with HREY content as high as 1100 ppm (Lou and Gu, 2020; Yang et al., 2021b; Zhang et al., 2021). Previous studies suggested that phosphorus enrichment in phosphorites was mainly associated with phosphorus-rich upwelling currents and began to accumulate in the Paleoproterozoic, continuing into the Phanerozoic (Glenn et al., 1994; Lehmann and

* Corresponding author at: State Key Laboratory of Ore Deposit Geochemistry, Institute of Geochemistry, Chinese Academy of Sciences, Guiyang 550081, China.
E-mail address: fanhaifeng@mail.gyig.ac.cn (H. Fan).

https://doi.org/10.1016/j.oregeorev.2022.105146
Received 13 May 2022; Received in revised form 26 September 2022; Accepted 5 October 2022
Available online 7 October 2022

Myrberg, 2008; Pufahl and Groat, 2017; Fathin et al., 2021). However, the potential REY sources (seawater, terrestrial, and hydrothermal) have not been well-determined.

Previous studies reported a modern seawater-like Hg isotope compositions (Δ^{199}Hg: 0.13–0.24 ‰; Δ^{200}Hg: 0.05–0.10 ‰) and Y/Ho ratios (45–60) in Zhijin phosphorites, and suggested a negligible hydrothermal REY source (Yin et al., 2017; Xing et al., 2021; Zhang et al., 2021). Therefore, we focus on whether the source is seawater or terrestrial in this study. The REY pattern of modern deep-sea mud is similar to that of modern seawater because the REY in its apatite is primarily derived from modern seawater (Kon et al., 2014; Liao et al., 2019). If REY in Zhijin phosphorite was derived directly from the seawater column, its pattern should be consistent with that of carbonate. However, REY pattern of Zhijin phosphorite exhibits obvious HREY depletion compared to those of Zhijin dolomite (Yang et al., 2021a; Yang et al., 2021b). At present, there is a debate as to whether the REY originated from seawater. Continental weathering might also play an important role in the material supply of seawater during the early Cambrian, which is evidenced by the higher $^{87}Sr/^{86}Sr$ ratios in early Cambrian seawater than Neoproterozoic seawater (Halverson et al., 2007; Li et al., 2013). Currently, ion adsorption-type REY deposits related to granites weathering and sedimentary-type REY deposits related to basalts weathering have been reported not only in South China but also in the rest of the world (Price et al., 1991; Zhou et al., 2013; Li et al., 2019; Borst et al., 2020). Similar REY deposits may have developed during the early Cambrian, and their erosion could supply significant REY into ancient ocean. The terrigenous REY also could be preserved in those clastic rocks (e.g., black shale), and can be recognized (Nesbitt and Young, 1982; Panahi and Young, 1997; Young, 2002; Ma et al., 2015).

Here, the Motianchong (MTC), Gaoshan (GS), Daga (DG), and Maoping (MP) phosphorite sections in the Zhijin area were investigated. We utilized the REY geochemistry and Sr isotopes to evaluate the contribution of seawater-sourced REY to REY enrichment in Zhijin phosphorites. Meanwhile, the trace element geochemistry and Nd isotopes of Zhijin phosphorites combined with the provenance of Zhijin shales to investigate the contribution of terrestrial sources to REY enrichment.

2. Geological setting

2.1. Paleogeography and granite distribution

During the Ediacaran-Cambrian transition, the Yangtze Platform gradually evolved into a passive continental margin basin (Wang and Li, 2003; Chen et al., 2009). The well-preserved Ediacaran to early Cambrian stratigraphic sequence of the South China Yangtze Platform includes three types of sedimentary facies: platform, transition, and deep-basin facies (Zhu et al., 2003). The platform facies was dominated by thick-layered carbonate strata, the deep-basin facies by black cherts and shales, and the transition zone (located in the area between the other two facies) by carbonates and black shales (Zhang et al., 2020). Large-scale economic phosphate ore deposits in the early Cambrian were associated with platform facies (Fig. 1) (Steiner et al., 2007). The Mesoproterozoic granites, which are mainly distributed in the southwestern margin of the Yangtze Platform, were intruded in Mesoproterozoic strata, including the Kunyang Group, Julin Group, Huili Group, and Dahongshan Group (Fig. 1) (Chen et al., 2021). Additionally, the Neoproterozoic granites also are mainly distributed in the margin of the Yangtze Platform, which were intruded in Huangshuihe Group, Sibaoan Shuangxiwu Group, Kunyang Group, Sibao Group, Shuangqiaoshan Group, Shangxi Group, Archean–Paleoproterozoic Kongling Complex, Kangding Complex, Suxiong Formation, Nannihu Formation, and Meiyaogou Formation (Fig. 1) (Zhu et al., 2019; Wang et al., 2010, and references therein).

2.2. Deposit geology and petrography

The Zhijin phosphorite ore deposit is located in southwest China, at the southwest end of the Qianzhong Uplift (Zhang et al., 2021). The main phosphate resources originate from the MTC, GS, DG, and MP ore

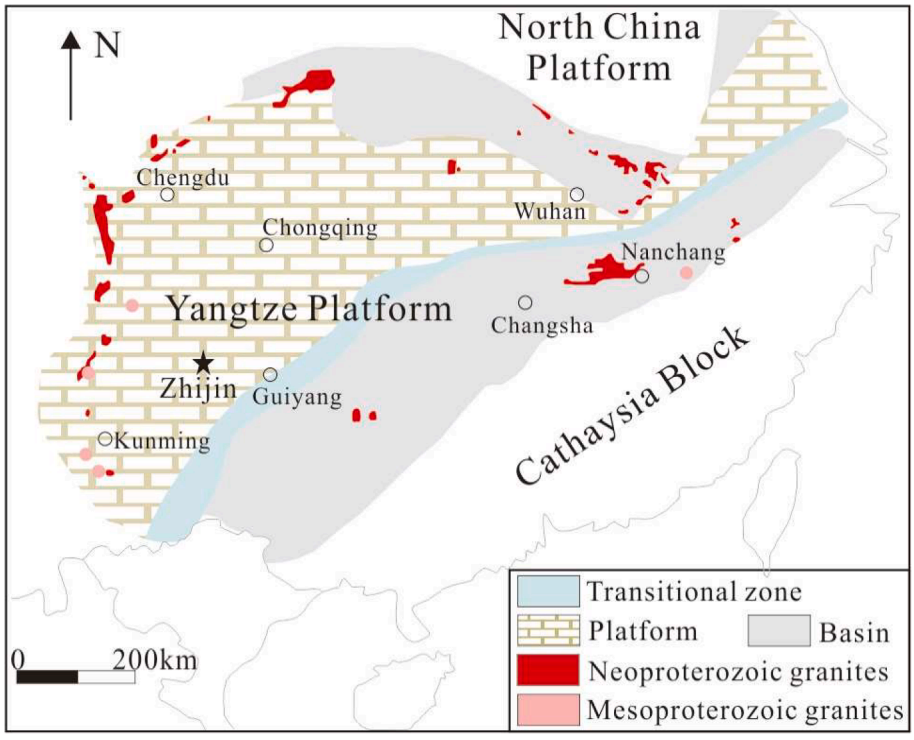

Fig. 1. Geological map of the Yangtze Platform, South China. Black pentagon represents study area. Modified from Zhu et al. (2014), Zhu et al. (2019), and Chen et al. (2021).

blocks (Fig. 2a). The Zhijin phosphorite ore deposit has a Rb-Sr isochron line age of 541 ± 12 Ma, which corresponds to that of tuff in the middle Zhongyicun Member (535.2 ± 1.7 Ma) (Shi, 2005; Zhu et al., 2009). Meanwhile, the black shale immediately overlain on Zhijin phosphorite has a Re-Os age of 522.9 ± 8.6 Ma (Wei et al., 2017). Taking the MTC section as an example, the Zhijin phosphorite ore body is strata-bound and spread northeast (58°) (Fig. 2b). It is mainly hosted by the Lower Cambrian Gezhongwu Formation underlain by siliceous dolostones of the Dengying Formation and overlain by black shales and feldspathic quartz sandstones of the Niutitang Formation (Fig. 2b) (Yang et al., 2021b). The stratigraphic sequence and spread of the remaining three phosphorite sections (GS, DG, and MP sections) is consistent with that of MTC section. The MTC section formed two different structure types. First, unequal-thickness interbedding between black phosphorite and grey phosphatic dolostone (Fig. 3a) or between black phosphorite and grey phosphorus-bearing dolostone (Fig. 3b) formed a wave structure. Black phosphorite is approximately 2–4 cm thick, while gray phosphatic dolostone or gray phosphorus-bearing dolostone is approximately 2–6 cm thick. In addition, a large number of lenticular (Fig. 3c) and cross-bedding structures (Fig. 3d) were observed in the hand specimens. Second, the unequal-thickness interbedding between black phosphorite and dark gray phosphorus-bearing dolostone (Fig. 3e) or between black phosphatic dolostone and dark gray phosphorus-bearing dolostone formed a parallel bedding structure (Fig. 3f). The black phosphorite or black phosphatic dolostone layer is approximately 1–4 cm thick, while the dark gray phosphorus-bearing dolostone layer is approximately 6 cm thick. Furthermore, the dark gray phosphorus-bearing dolostone is interbedded with thin black phosphorite, forming a laminar structure (Fig. 3h) with 0.1–0.5 cm thick laminations (Fig. 3g, h). The structure types of DG section are consistent with that of MTC section. However, the GS and MP sections only exhibit parallel bedding structures and laminar structures.

Drillings from the prospecting section show a coordinated change in the P_2O_5 and rare earth oxide (RE_2O_3) contents (Fig. 2b). Fluorapatite

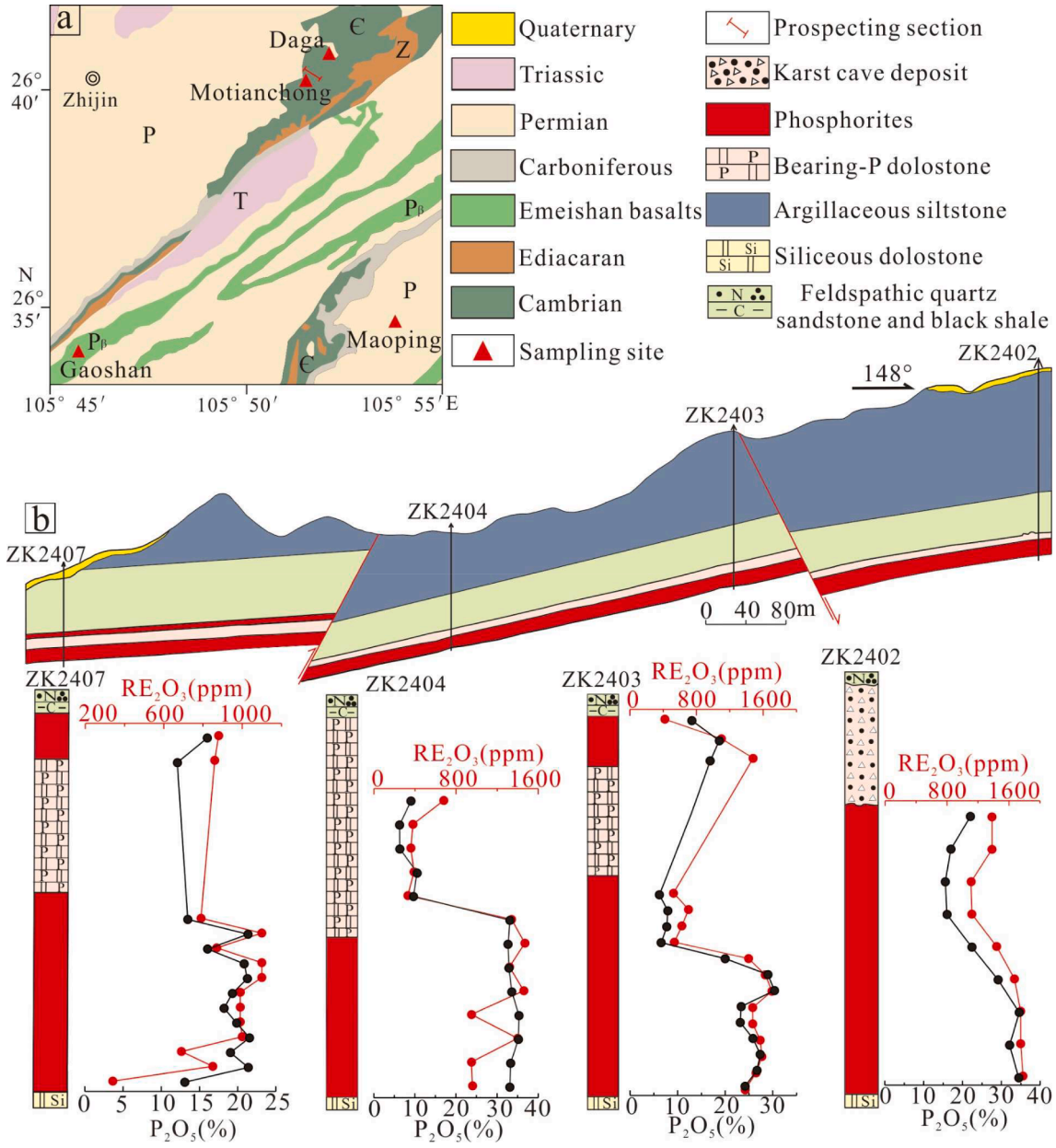

Fig. 2. **a** Geological map of the Zhijin region. **b** Prospecting section from the Motianchong phosphorite deposit, wherein the embedded curves show a positive correlation between P_2O_5 and Rare Earth Oxide (RE_2O_3) in the prospecting section.

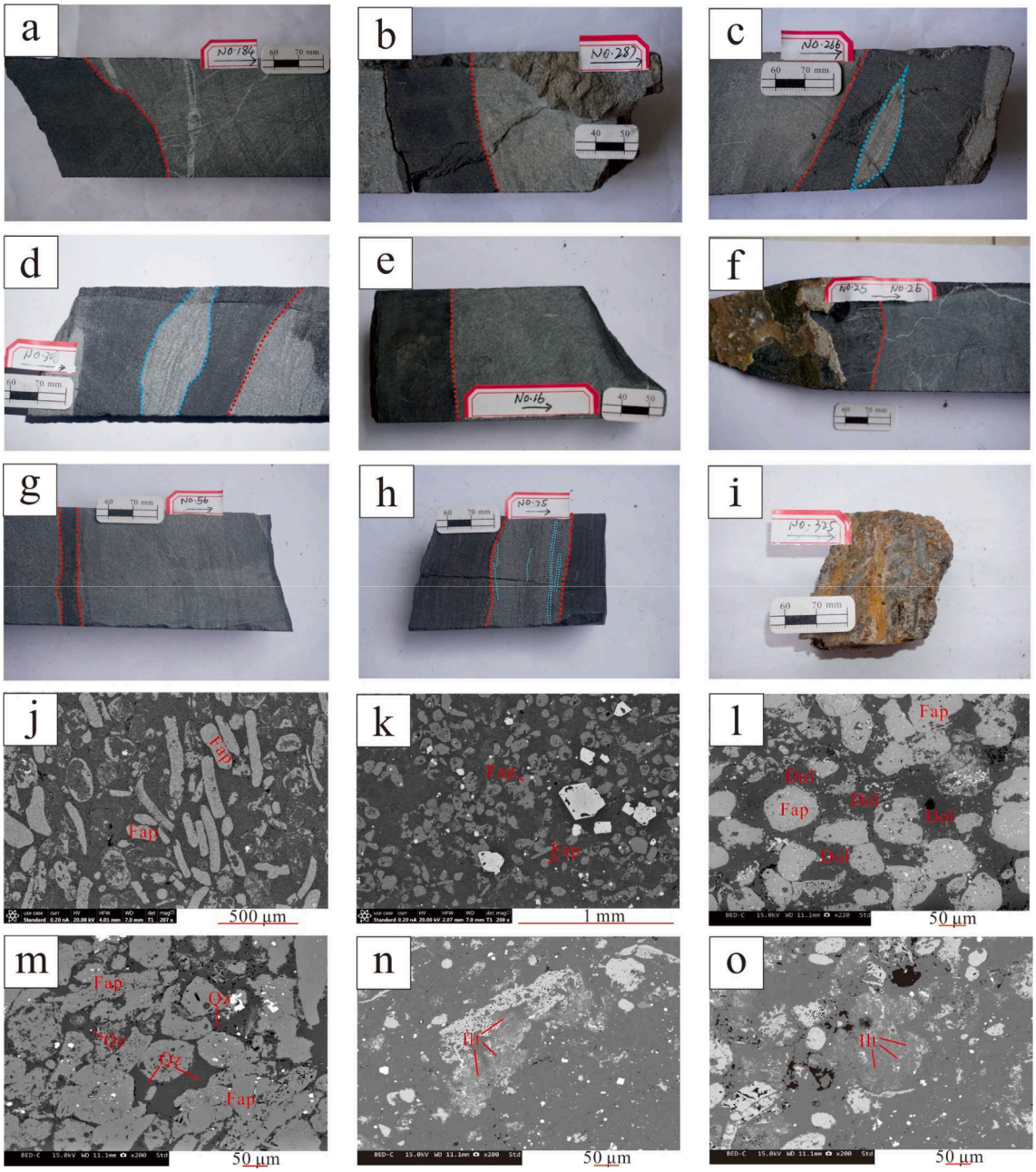

Fig. 3. Deposit structure maps. **a** An unequal-thickness interbedding between black phosphorite and gray phosphatic dolostone formed wave structure. **b** An unequal-thickness interbedding between black phosphorite and gray phosphorus-bearing dolostone formed wave structure. **c** A large number of lenticular structures (blue lines). **d** Cross-bedding structures (blue lines). **e** An unequal thickness interbedding between black phosphorite and dark gray phosphorus-bearing dolostone formed parallel bedding structure. **f** An unequal thickness interbedding between black phosphatic dolostone and dark gray phosphorus-bearing dolostone formed parallel bedding structure. **g, h** Parallel bedding structure (red lines). **h** Thin laminar structures (blue lines). **i** Paleo-weathering crust. **j** Biogenic intraclast fluorapatites (Fap). **k** Biochemical spherical fluorapatites (Fap). **l** Dolomite (Dol) cement between fluorapatites. **m** Quartz (Qz) cement between fluorapatites. **n** Illite (Ilt) cement between fluorapatites. **n, o** Illites (Ilt) of poor roundness. (For interpretation of the references to colour in this figure legend, the reader is referred to the web version of this article.)

can be classified into biogenic intraclasts (Fig. 3j) and biochemical spherical particles (Fig. 3k). The lengths of biogenic intraclasts range from approximately 120 to 500 μm, while the diameters of the biochemical spherical particles range from 35 to 140 μm. Dolomite, quartz, and illite are the three main types of cements between fluorapatites (Fig. 3 l, m, n, o), wherein the illites exhibit poor-roundness characteristics, with diameters ranging from 70 to 200 μm (Fig. 3n, o).

3. Samples and analytical methods

3.1. Sampling

We selected representative samples of black shales and phosphorites from MTC, GS, DG, and MP sections in the Zhijin phosphorite ore deposit (Fig. 2a). After sampling, the possible weathering crust and alteration veins were removed, and the samples were washed, dried, milled to 200 mesh, and finally dried for experimental analysis.

3.2. Analytical methods

For the major element analysis, samples were accurately weighed (~0.7 g), placed into a platinum crucible, and melted at 1050 °C with a mixed flux ($Li_2B_4O_7$-$LiBO_2$-$LiNO_3$). The major elements were determined using an X-ray fluorescence spectrometer at ALS Minerals Co. ltd. (Guangzhou, China). Another dried sample was simultaneously and accurately weighed, aerobically burned at 1000 °C in a muffle furnace, and finally accurately weighed after cooling. The weight difference between the samples before and after burning was defined as the limiting oxygen index (LOI). GBW07211, GBW07237, and GBW07241 were used as standard materials to validate the data. The relative deviation of the precision control was <7.5 %, and the relative error of the accuracy was <7.5 % during the testing for each element.

For the trace element and REY analysis, the sample (0.1 g) was first added to a lithium borate flux ($LiBO_2/Li_2B_4O_7$) and melted in a furnace at 1025 °C. After the melt cooled, it was dissolved in nitric acid, hydrochloric acid, and hydrofluoric acid, and the volume was fixed, then analyzed using plasma mass spectrometry (ICP-MS) at ALS Minerals Co. ltd. (Guangzhou, China). OREAS-100a, OREAS-120, and STSD-1 were used as standard materials to validate the data. The relative deviation of the precision control was < 10 %, and the relative error of accuracy was < 10 % during the testing of each trace element. The anomalies of Ce/Ce*, Eu/Eu*, and Pr/Pr* in Zhijin phosphorites were calculated using $Ce/Ce^* = Ce_N/(La_N*Pr_N)^{1/2}$, $Eu/Eu^* = Eu_N/(Sm_N*Gd_N)^{1/2}$, and $Pr/Pr^* = 2*Pr_N/(Ce_N + Nd_N)$, respectively.

We used the field-emission scanning electron microscope (SEM) to observe the minerals' microstructures. The electron beam emitted by the electron gun was converted into a high-energy electron beam of 10–30 kV, which was focused into a 1 μm microbeam to bombard the mineral surface to collect backscattered electron images (BSE). Additionally, we used the Electron Probe Microanalyzer (EPMA) to analyze the major element compositions of dolomite, quartz, and illite. For elemental analysis, the operating voltage and beam spot diameter of the instrument were 15 kV and 5 μm, respectively. Only the dolomite was analyzed at 10 nA current; the other two minerals were analyzed at 20 nA current. The analysis error was <2 %.

Approximately 50 mg of sample powder was weighed and dissolved in nitric acid, hydrochloric acid, and hydrofluoric acid for the whole-rock Sr and Nd isotopes analysis. Sr isotopic compositions were determined using MC-ICP-MS at Wuhan Sample Solution Analytical Technology Co., ltd., following the method of Li et al. (2012). The measured result for the standard BCR-2 was $^{87}Sr/^{86}Sr$ 0.704999 ± 0.000007 (2σ). Nd isotopic compositions were determined using TIMS at the Institute of Geochemistry, Chinese Academy of Sciences (CAS), Guiyang, following the method of Li et al. (2016). The measured result for the standard BCR-2 was $^{143}Nd/^{144}Nd$ 0.512651 ± 0.000001 (2σ). Finally, for the analysis of total inorganic content (TIC) in Zhijin shale, first, we accurately weighed the sample, and analyzed the total carbon content (TC) using an infrared sensor. Then we used hydrochloric acid to remove carbonate from the sample, and then washed the sample to neutral pH in deionized water. After drying, the organic carbon content (TOC) of the sample was measured using an infrared sensor. The TIC content in the sample was defined as the difference between TC and TOC (TIC = TC – TOC). GSD-9 was used as the standard material to validate the data.

4. Results

The major element, trace element, REY, and TIC contents of Zhijin phosphorites and black shales are listed in Tables 1 and 2, and Supplementary table. The EPMA data of dolomite, quartz, and illite are listed in Supplementary table. The REY was normalized by Post-Archean Australian shale (PAAS) (McLennan, 1989). The average P_2O_5 contents of phosphorites from the four sections are 26.3–30.1 %, and the average REY contents of phosphorites are 1,408–1,491 ppm. The PAAS-normalized REY patterns in all Zhijin phosphorites exhibit negative Ce anomalies and HREY depletions (Wu et al., 2022), which differ from HREY enrichment of Zhijin dolomites, deep-sea mud, and modern seawater (Fig. 4a, b) (Nozaki and Alibo, 2003; Liao et al., 2019; Lou and Gu, 2020). The Ce anomalies are true in Zhijin phosphorites; meanwhile,

Table 1
Contents of major (%), trace element (ppm) and REY (ppm) in Zhijin phosphorites. Some of the MTC data come from Wu et al. (2022).

	MTC section			GS section			DG section			MP section		
	n = 50			n = 9			n = 31			n = 29		
	Average	min	max	Average	min	max	Average	min	max	Average	min	max
La	318	117	504	289	71.5	458	313	151	474	291	194	418
Ce	200	83.1	378	230	99.0	372	223	99.0	338	214	154	308
Pr	54.9	21.7	99.3	49.2	13.5	82.6	54.9	26.1	83.6	52.5	38.2	76.0
Nd	236	96.7	435	196	58.6	345	218	101	352	233	169	334
Sm	42.9	17.2	80.0	38.6	11.3	66.3	44.4	18.4	71.5	43.2	31.0	62.0
Eu	9.44	3.89	17.2	8.39	2.66	13.7	10.3	5.21	15.8	11.5	8.49	15.7
Gd	51.2	20.8	96.7	43.2	13.0	72.6	49.2	23.2	70.2	51.1	36.3	70.4
Tb	6.95	2.97	12.9	6.60	1.93	11.5	7.42	3.49	10.6	6.86	4.89	9.40
Dy	42.3	18.7	75.7	38.7	11.8	63.4	43.3	20.6	60.6	40.6	28.9	54.6
Y	476	191	741	464	134	745	478	250	679	451	325	623
Ho	9.06	3.97	15.6	7.95	2.39	13.8	8.73	4.30	12.3	8.44	5.93	11.3
Er	23.5	10.2	39.8	20.3	6.13	34.5	22.1	11.4	31.8	21.4	15.1	28.8
Tm	2.73	1.23	4.50	2.49	0.82	4.15	2.72	1.40	3.99	2.47	1.68	3.32
Yb	12.8	5.80	20.8	12.6	4.44	19.4	13.6	7.67	19.0	11.2	7.47	14.7
Lu	1.65	0.73	2.46	1.53	0.56	2.39	1.67	0.93	2.41	1.45	0.94	1.94
Zr	37.3	10.0	132	36.8	14.0	60.0	36.9	9.0	118	28.4	14.0	51.0
P_2O_5	29.8	19.1	37.5	26.3	20.6	32.9	30.1	11.7	38.3	27.0	18.3	35.3
∑REY	1488	626	2523	1408	431	2304	1491	748	2185	1440	1045	2030
Y/Ho	53	45	59	59	54	63	55	47	63	53	50	56
Er/Nd	0.10	0.09	0.12	0.11	0.09	0.12	0.10	0.09	0.13	0.09	0.08	0.11
Ce/Ce*	0.35	0.31	0.44	0.47	0.42	0.74	0.40	0.35	0.48	0.40	0.38	0.44
Eu/Eu*	0.95	0.88	1.09	0.98	0.93	1.09	1.05	0.92	1.27	1.16	1.03	1.30
Pr/Pr*	1.31	1.24	1.36	1.27	1.02	1.37	1.35	1.22	1.44	1.24	1.19	1.28
Dy_N/Sm_N	1.18	1.06	1.32	1.22	1.11	1.38	1.17	0.97	1.33	1.12	1.02	1.25
Sm_N/Yb_N	1.69	1.46	2.00	1.50	1.28	1.80	1.64	1.18	2.25	1.97	1.63	2.39
Gd_N/Yb_N	2.40	2.05	2.84	2.02	1.76	2.35	2.17	1.77	2.63	2.77	2.41	3.33
La_N/Sm_N	1.08	0.82	1.26	1.10	0.92	1.24	1.04	0.74	1.22	0.98	0.80	1.07
La_N/Yb_N	1.83	1.48	2.03	1.65	1.19	1.87	1.68	1.41	1.92	1.92	1.59	2.11

Table 2
Major (%), trace (ppm), REY compositions (ppm), and total inorganic (TIC) contents (%) of Zhijin shales and granites of different ages. The granite data are taken from Li et al. (2003), Liu et al. (2019), and Huang et al. (2021).

Samples	Al_2O_3	CaO	Na_2O	K_2O	P_2O_5	LOI	SiO_2	TIC	La	Th	Sc	CIA
MTC shale-1	7.35	30.40	0.04	2.27	22.50	6.15	24.48	0.315	46.1	6.10	5.2	74
MTC shale-2	14.63	0.74	0.04	4.34	0.27	11.83	60.58	0.184	34.7	12.60	12.4	75
MTC shale-3	11.83	4.22	0.02	3.78	0.52	10.76	61.49	1.297	24.0	10.15	8.9	74
GS shale-1	1.01	8.90	0.03	0.34	5.58	27.85	7.34	0.210	26.2	1.20	1.7	68
GS shale-2	8.34	6.37	0.05	2.99	3.53	9.64	61.71	0.951	35.8	7.35	8.4	71
DG shale-1	16.47	0.33	0.04	5.16	0.22	11.06	57.76	0.122	49.2	13.53	17.3	74
DG shale-2	12.05	6.03	0.04	3.61	3.27	21.79	40.28	0.087	54.9	10.30	11.9	75
MP shale-1	13.15	2.48	0.07	4.21	0.23	11.91	59.64	0.905	32.7	9.74	13.4	73
MP shale-2	14.08	4.01	0.06	4.56	2.61	10.89	55.88	0.032	47.8	11.35	14.3	73
Cambrian granites(n = 11)	12.41	0.42	4.44	3.14	0.02	0.89						
Neoproterozoic granites(n = 9)	12.56	0.59	3.45	3.38	0.12	1.50						
Mesoproterozoic granites(n = 10)	12.66	0.47	2.83	5.13	0.04	0.58						

they do not exhibit good correlations with Eu/Eu*, REY contents, and Dy_N/Sm_N ratios, respectively (Fig. 5) (Wu et al., 2022). Zhijin phosphorites exhibit a negative correlation between Y/Ho and Sm_N/Yb_N values, and Y/Ho values of carbonates in Zhijin phosphorites lie between the seawater and terrestrial values (Fig. 6a) (Abedini and Calagari, 2017; Xing et al., 2021; Wu et al., 2022). Zhijin phosphorites also exhibit a negative correlation between Y/Ho ratios and Zr contents (Fig. 6b) (Wu et al., 2022). The average La_N/Yb_N values of Zhijin phosphorites are 1.83, 1.65, 1.68, and 1.92 in the MTC, GS, DG, and MP sections, respectively (Fig. 6c) (Xu et al., 2019; Xing et al., 2021; Yang et al., 2021b; Wu et al., 2022). The average La_N/Sm_N values of Zhijin phosphorites are 1.08, 1.10, 1.04, and 0.98 in the MTC, GS, DG, and MP sections, respectively (Fig. 6c) (Xu et al., 2019; Xing et al., 2021; Yang et al., 2021b; Wu et al., 2022). In addition, La_N/Yb_N ratios of Zhijin phosphorites are higher than those of modern seawater and deep-sea mud, while its La_N/Sm_N ratios are consistent with those of modern seawater and deep-sea mud (Fig. 6c) (Liao et al., 2019; Xu et al., 2019; Xing et al., 2021; Yang et al., 2021b; Wu et al., 2022). In general, REY contents of Zhijin phosphorites exhibit a positive correlation with their P_2O_5 contents (Fig. 6d) (Xu et al., 2019; Xing et al., 2021; Yang et al., 2021b; Wu et al., 2022).

To determine the materials' provenance in Zhijin paleo-seawater, we chose Zhijin black shales immediately overlain on the Zhijin phosphorite ore deposit, and the provenance was evaluated by trace elements and chemical alteration index (CIA) diagrams (Fig. 8) (Nesbitt and Young, 1984; Cullers and Podkovyrov, 2000). In Zhijin shales, the contents of Al_2O_3, CaO, Na_2O, K_2O, P_2O_5, SiO_2, and TIC are in the range of 1.01–16.47 %, 0.33–30.40 %, 0.02–0.07 %, 0.34–5.16 %, 0.22–22.50 %, 7.34 %–61.71 %, and 0.032–1.297 % respectively. Meanwhile, its REY, La, Th, and Sc contents are 75.2–897 ppm, 24.0–54.9 ppm, 1.20–13.53 ppm, and 1.7–17.3 ppm, respectively. Except for one shale sample which contains REY content of 897 ppm, the other shales have an average REY content of 185 ppm. The Sr-Nd isotopic compositions of Zhijin phosphorites are listed in Tables 3 and 4. The $^{87}Sr/^{86}Sr(i)$ values of Zhijin phosphorites are 0.7087–0.7091, 0.7077–0.7088, 0.7088–0.7092, and 0.7087 in the MTC, GS, DG, and MP sections, respectively. Meanwhile, the $^{87}Sr/^{86}Sr(i)$ values of Zhijin phosphorites exhibit positive correlations with their Sr and REY contents (Fig. 7) (Liu and Zhou, 2020). The $\varepsilon_{Nd}(t)$ values of Zhijin phosphorites are −7.3 – −6.8, −8.4 – −7.3, −8.6 – −7.2, and −7.4 – −7.1 in the MTC, GS, DG, and MP sections, respectively. In addition, the two-stage Nd model ages (T_{2DM}) of Zhijin phosphorites range from 1.8 to 2.0 Ga (Fig. 9).

5. Discussion

5.1. Contribution of seawater-sourced REY

5.1.1. REY geochemistry

REY geochemical characteristics can constrain sedimentary and diagenetic conditions, particularly as effective indicators of REY sources in marine phosphorite (German and Elderfield, 1990; Jarvis et al., 1994; Shields and Stille, 2001; Picard et al., 2002). REY pattern of Zhijin phosphorites exhibits obvious HREY depletion compared to Zhijin dolomite and modern seawater (Fig. 4a, b) (Nozaki and Alibo, 2003; Lou and Gu, 2020; Wu et al., 2022). The result of leaching experiment showed that MREY was preferentially leached compared to LREY and HREY in phosphatic shales (Hannigan and Sholkovitz, 2001), indicating that residual samples should have exhibited enrichment in LREY and HREY (Mcarthur and Walsh, 1984). Therefore, HREY depletion in Zhijin phosphorites could not result from late surface weathering; this confirmation ensured the representative nature of the samples. Furthermore, the anomalous La enrichment can lead to overestimation of Ce anomaly, which can be assessed using a scatter diagram of Pr/Pr* versus Ce/Ce* (Bau and Dulski, 1996). Zhijin phosphorites exhibit real Ce anomalies in this study (Fig. 5a) (Wu et al., 2022). Meanwhile, diagenesis can compel Ce anomalies to exhibit a negative correlation with Eu anomalies and Dy_N/Sm_N ratios (Shields and Stille, 2001). It also can result in a positive correlation between Ce anomalies and REY contents (Shields and Stille, 2001). However, these phenomena are not found in Zhijin phosphorites (Fig. 5b, c, d) (Liu et al., 2020; Gong et al., 2021; Yang et al., 2021a; Zhang et al., 2021; Wu et al., 2022). In summary, late diagenetic and subsequent surface weathering processes did not seem to alter the REY patterns in Zhijin phosphorites.

Yttrium (Y) has much lower marine particle reactivity than Ho (Bau et al., 1997; Nozaki et al., 1997), and its mean oceanic residence time is approximately 1.8 times greater than Ho (Bau et al., 1997; Nozaki et al., 1997). Y is also less effectively scavenged from seawater than Ho, causing a higher Y/Ho ratio in seawater than in continental crust (Bau et al., 1997; Nozaki et al., 1997). The Y/Ho ratio has been used as an important indicator in tracing REY sources, as the Y/Ho ratio of terrestrial source is approximately 28 and the Y/Ho ratio of seawater source is approximately 60 (Abedini and Calagari, 2017). The Y/Ho ratios of Zhijin phosphorites from the four sections range from 45 to 63 (Wu et al., 2022). All of Zhijin phosphorites have Y/Ho ratios similar to the seawater source (Fig. 6a) (Xing et al., 2021; Wu et al., 2022). Therefore, our data indicates a contribution from seawater-sourced REY.

The PAAS-normalized REY patterns in sedimentary phosphates are typically employed to interpret REY behavior in seawater (Lécuyer et al., 2004; Garnit et al., 2012; Joosu et al., 2015; Gadd et al., 2016). The REY pattern in apatite could reflect an adsorption mechanism governed by surface crystal chemistry, and a substitution mechanism governed by bulk crystal-chemical properties (Reynard et al., 1999; Gadd et al., 2016). Compared to HREY, LREY was preferentially adsorbed on apatite surfaces, primarily in early diagenetic stage (Reynard et al., 1999). However, uptake of MREY in apatite affected by the substitution mechanism was higher than that of LREY and HREY, and primarily occurred in late diagenesis or deeper burial stages (Reynard et al., 1999). A La_N/Sm_N-La_N/Yb_N diagram was used to interpret mechanisms that led to REY uptake into apatite crystal lattice (Reynard et al., 1999). Based on the results of this and previous studies, the La_N/Yb_N and $La_N/$

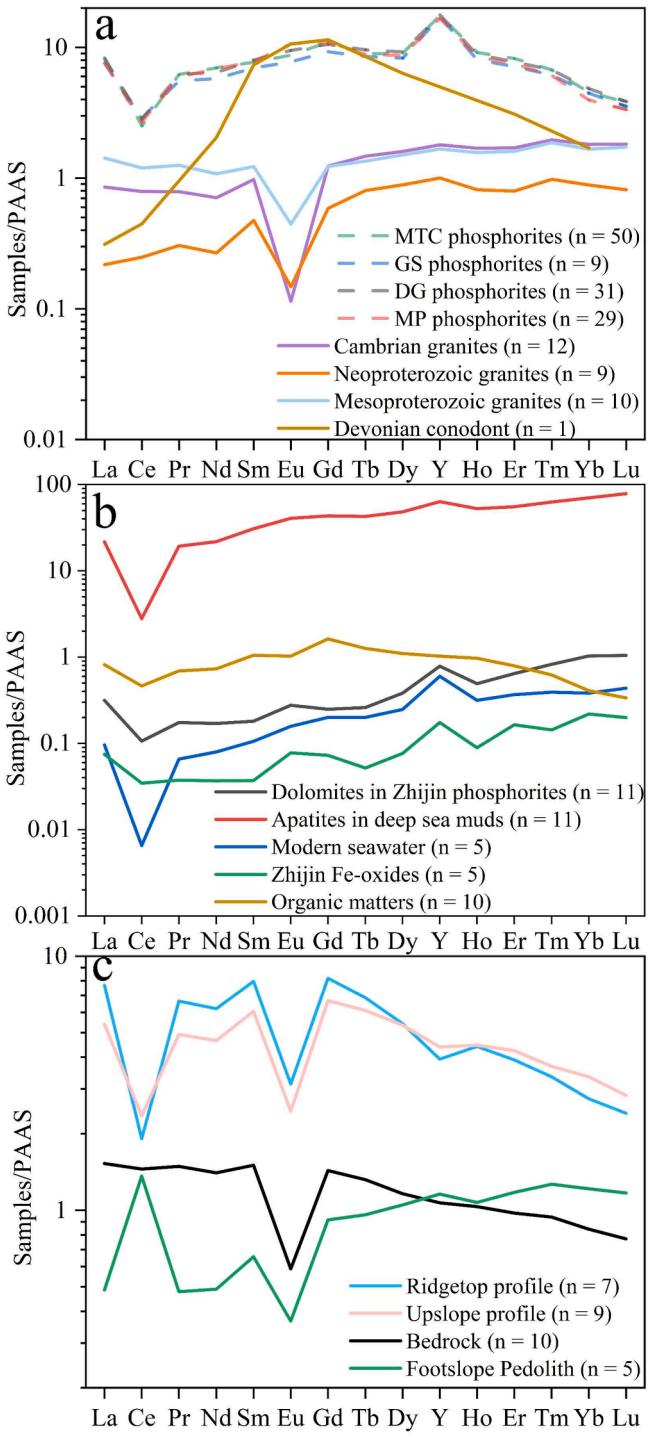

Fig. 4. PAAS-normalized REY patterns from different samples (McLennan, 1989). REY contents of MTC, GS, DG, and MP phosphorites are from this study. Some of the MTC data come from Wu et al. (2022). REY data of granite are from Li et al. (2003), Liu et al. (2019), and Huang et al. (2021). REY data of dolomite in Zhijin phosphorites are from Lou and Gu (2020). REY data of apatite in deep sea muds are from Liao et al. (2019). REY data of modern seawater are from Nozaki and Alibo (2003). REY data from the ridgetop profile, upslope profile, footslope pedolith and bedrock are from Li et al. (2020).

Sm_N values of Zhijin phosphorites are 0.82–2.11 and 0.54–1.26, respectively (Xu et al., 2019; Xing et al., 2021; Yang et al., 2021b; Wu et al., 2022). These values are inconsistent with that of Devonian conodont influenced by late diagenesis (Fig. 4a, 6c) (Grandjean-Lécuyer et al., 1993). Therefore, the REY patterns of Zhijin phosphorites were not altered by late diagenetic processes, indicating that REY patterns of HREY depletion in Zhijin phosphorites were inherited from ambient water during early diagenesis. It is suggested that the release of REY from Fe-oxide or organic matter was beneficial to REY enrichment in pore water under the interface between seawater and sediment during early diagenesis (Haley et al., 2004; Jiang et al., 2007). This may result in a REY pattern of HREY depletion in pore water (Haley et al., 2004; Jiang et al., 2007). Then REY in pore water entered into the apatite lattice ($REY^{3+} + Na^{+} \rightarrow 2Ca^{2+}$ and/or $REY^{3+} + Si^{4+} \rightarrow Ca^{2+} + P^{5+}$) (Liao et al. 2019). However, REY pattern of Zhijin Fe-oxide exhibits a negative Ce anomaly and HREY enrichment, which corresponds with that of modern seawater and Zhijin dolomite (Fig. 4b) (Nozaki and Alibo, 2003; Lou and Gu, 2020; Zhang et al., 2022). Furthermore, although organic matter in nearly contemporary shale exhibits REY pattern of MREY enrichment and HREY depletion, negative Ce anomaly indicates that organic matter was derived from phytoplankton of surface seawater (Fig. 4b) (Pi et al., 2013; Shields-Zhou and Zhu, 2013). Organic matter would preferentially adsorb MREY before sinking to the seawater-sediment interface (Kidder and Eddy, 1994). The Zn isotopes evidenced that Zhijin and Xia'an phosphorites had higher productivity levels than Meishucun phosphorites (Zhang et al., 2022). However, Xia'an phosphorites have very low REY contents (average 92 ppm), suggesting that organic matter was not the key factor leading to the extraordinary REY enrichment in Zhijin phosphorites (Zhang et al., 2022). In general, both Fe-oxide and organic matter represent REY cycling at the seawater member. In addition, REY pattern of modern seawater exhibits a negative Ce anomaly and HREY enrichment (Fig. 4b) (Nozaki and Alibo, 2003). The REY patterns and La_N/Sm_N and La_N/Yb_N values of apatites from deep-sea muds are consistent with those of modern seawater (Fig. 4b, 6c), which indicate that REY in deep-sea muds came directly from ambient water during early diagenesis (Kon et al., 2014; Liao et al., 2019). A previous study also suggested that there was no absolute time gap between HREY enrichment and HREY depletion in seawater, and REY pattern of seawater during geological history is consistent with that of modern seawater (Shields and Webb, 2004). Therefore, REY pattern of Zhijin Cambrian seawater also should have exhibited HREY enrichment, because REY pattern of Zhijin dolomite corresponds to those of modern seawater and apatite in deep-sea mud (Fig. 4b) (Nozaki and Alibo, 2003; Liao et al., 2019; Lou and Gu, 2020). However, REY pattern of HREY depletion in Zhijin phosphorite may indicate that REY from other sources (e.g., terrestrial) was mixed with seawater-sourced REY.

5.1.2. Sr isotopes

The seawater has a homogenous $^{87}Sr/^{86}Sr$ ratio because of a longer Sr residence time (~3–5 Ma) compared to the seawater's mixing time (~10^3 years) (Halverson et al., 2007). The $^{87}Sr/^{86}Sr$ composition (0.7091) of modern ocean primarily reflects a combination of the $^{87}Sr/^{86}Sr$ values from continental crust weathering (~0.7120) and submarine hydrothermal alteration (~0.7035) (Edmond, 1992). Owing to a noteworthy $^{87}Sr/^{86}Sr$ composition difference in the two main Sr sources, the $^{87}Sr/^{86}Sr$ value of seawater can track variations in continental crust weathering and submarine hydrothermal flux (Richter et al., 1992). Furthermore, marine carbonate and phosphate can inherit the $^{87}Sr/^{86}Sr$ composition of seawater (Kuznetsov et al., 2018). For instance, Sr isotopes have been used to study fish teeth to trace the isotopic composition of seawater (Ingram et al., 1994; Ingram, 1995). Additionally, Sr isotopes could be altered by meteoric diagenesis and dolomitization, which can increase Mn/Sr ratios to more than 2 (Kaufman and Knoll, 1995; Jacobsen and Kaufman, 1999). The Mn/Sr ratios range from 0.04 to 0.59 in Zhijin phosphorites (Table 3), indicating that Sr isotopes of Zhijin phosphorites recorded true seawater information. The $^{87}Sr/^{86}Sr(i)$ ratios range from 0.7085 to 0.7092 in Zhijin phosphorites, which are consistent with Cambrian seawater (0.7080–0.7090) (Derry et al., 1994; McArthur et al., 2001; Halverson et al., 2007). Previous Sr isotope values of Zhijin phosphorites from the MTC ore block

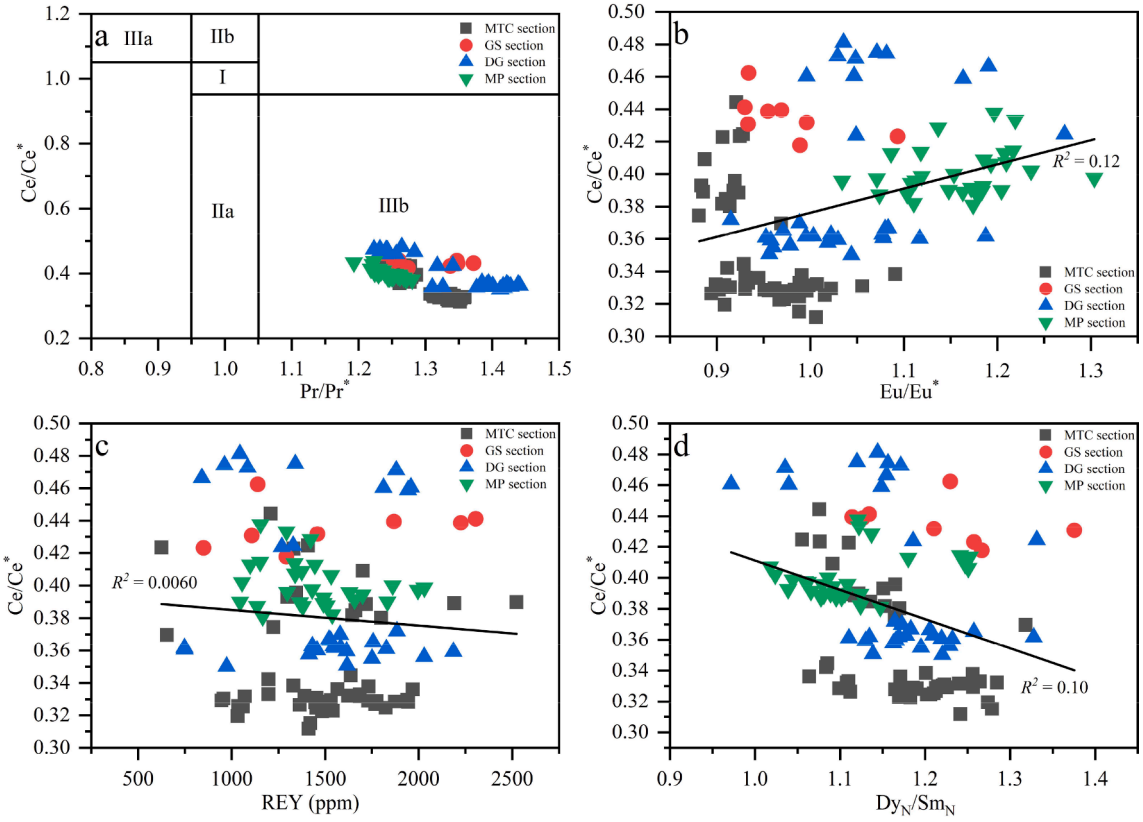

Fig. 5. Scatter plots of different REY parameters in Zhijin phosphorites. **a** Ce/Ce* vs Pr/Pr* diagram, wherein I represents no anomaly, IIa represents negative Ce anomaly caused by positive La anomaly, IIb represents positive Ce anomaly caused by negative La anomaly, IIIa represents a true positive Ce anomaly, IIIb represents a true negative Ce anomaly. **b** Ce/Ce* vs Eu/Eu* diagram. **c** Ce/Ce* vs REY diagram. **d** Ce/Ce* vs Dy_N/Sm_N diagram. Some of the MTC data come from Wu et al. (2022).

were also between 0.7074 and 0.7109 (Liu and Zhou, 2020; Zhang et al., 2021). This suggests that Zhijin phosphorite REY was partially derived from Cambrian seawater.

5.2. Terrestrial source contributions

5.2.1. Provenance and geochemistry of Zhijin sedimentary rocks

The final assembly of Gondwanaland resulted in extensive continental collisions at 540 Ma, causing widespread erosion and terrestrial sedimentation (Li et al., 2013). A large number of eroded materials were preserved in northern Africa, across the Himalayas, South China, and eastern Australia (Li et al., 2013). Positive $^{87}Sr/^{86}Sr$ excursions have also been observed in other locations during the early Cambrian (Sawaki et al., 2008; Melezhik et al., 2009). The highest Sr isotopic values have also been recorded in Cambrian seawater (Halverson et al., 2007). Meanwhile, the $^{87}Sr/^{86}Sr(i)$ values of Zhijin phosphorites exhibit positive correlations with their Sr and REY contents (Fig. 7) (Liu and Zhou, 2020). Therefore, continental weathering could bring abundant REY into Zhijin seawater. Next, we evaluated the importance of terrigenous sources for REY enrichment in Zhijin phosphorites.

The chemical compositions of terrigenous clastic rocks largely represent the specific combination of different types of rocks (McLennan et al., 1993). The provenance of siliceous clastic rocks can be distinguished by the least-mobile elements (Wronkiewicz and Condie, 1987; Nesbitt and Markovics, 1997). This is particularly true for Al, Th, Sc, REY, and Nd isotopes (Wronkiewicz and Condie, 1987; Nesbitt and Markovics, 1997), which suggests that some high field strength elements (including La, Th, Sc, and Zr) can be used to reconstruct provenance because silicic rocks are more enriched in La and Th and more depleted in Sc than basic rocks (Bhatia and Crook, 1986; Cullers, 1994; Cullers and Podkovyrov, 2000). Thus, we selected black shales that deposited immediately after Zhijin phosphorites at the top of Gezhongwu Formation to better understand the Zhijin paleo-seawater material provenance. The La-Th-Sc diagram (Fig. 8a) suggests that clastic materials in Zhijin paleo-seawater were derived from granodiorite to granite (Li et al., 2003; Liu et al., 2019; Huang et al., 2021).

The chemical alteration index (CIA) can quantitatively determine the weathering degree of the provenance of clastic rocks (Nesbitt and Young, 1982). The CIA has also been used to investigate the sediments' provenance (Panahi and Young, 1997; Young, 2002). The proportions of plagioclase and potassium feldspar are good indicators of possible source rock types of clastic sedimentary rocks (Fedo et al., 1995). In the diagram of Al_2O_3-CaO*+Na_2O-K_2O (A-CN-K), the proportion can be determined by analyzing the intersection location between the data trend line and the blended line connecting the feldspar (Nesbitt and Young, 1984). The intersection location likely represents an unweathered provenance (Nesbitt and Young, 1984). It has been suggested that weathering caused the transformation of feldspar into clay minerals, such as smectite, which can also move towards becoming kaolinite and gibbsite (Tosca et al., 2010). The weathering of provenance led to a gradual accumulation of Al and depletion of easily transportable elements such as Ca, Na, and K in the remaining weathering material (Nesbitt and Young, 1982, 1989; Fedo et al., 1995; Nesbitt and Markovics, 1997). These processes can be observed in the A-CN-K diagram (Fig. 8b) (Nesbitt and Young, 1984). The Al_2O_3, CaO*, Na_2O, and K_2O mole values are represented in the A-CN-K diagram, wherein the CaO* represents the silicate component ($CaO^* = mol\ CaO - mol\ CO_{2\ calcite} - (1/2 \times mol\ CO_2)_{dolomite} - (10/3 \times mol\ P_2O_5)_{apatite}$) (Fedo et al., 1995). Owing to the low-carbonate contents of Zhijin shales (TIC, 0.032–1.297 %) (Table 2), CaO was corrected using the mole value of P_2O_5. If the mole values of CaO* were lower than that of Na_2O, the CaO* components were reliable (McLennan et al., 1993). If the mole values of CaO*

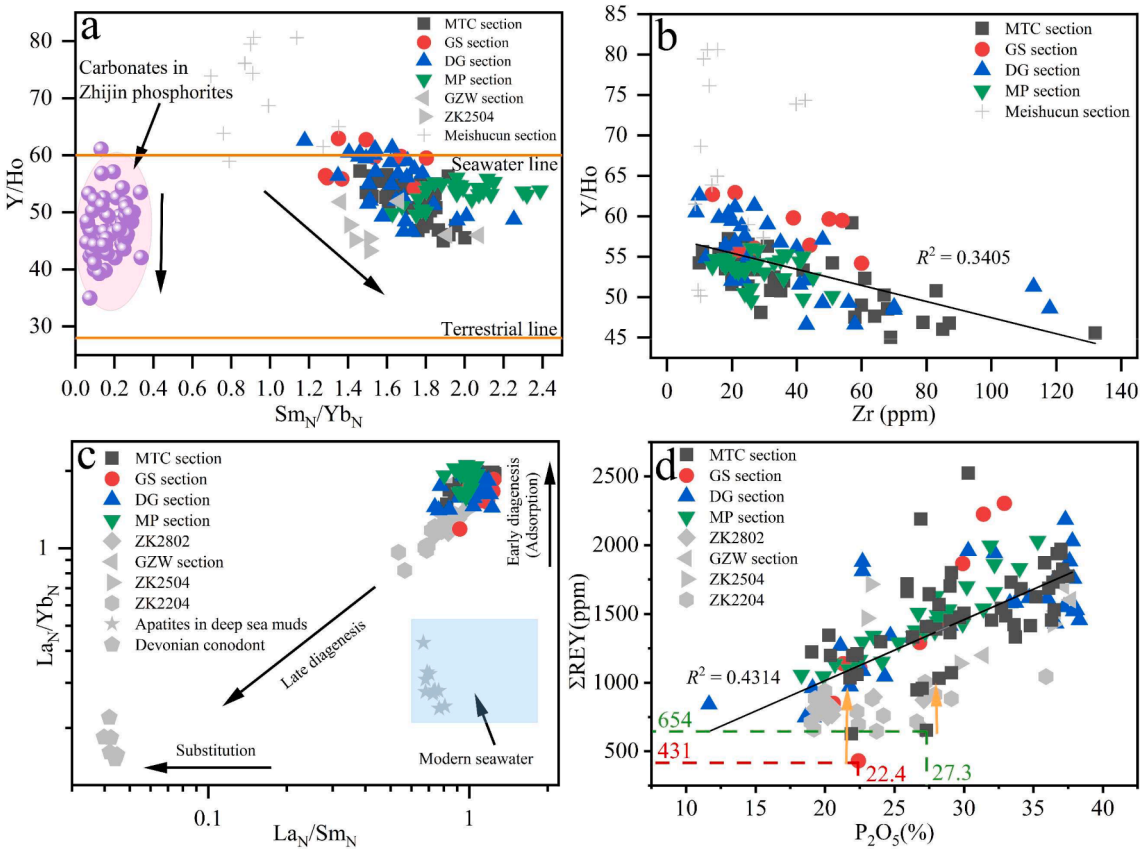

Fig. 6. Plots for various parameters in Zhijin phosphorites. **a** Sm_N/Yb_N vs Y/Ho diagram. **b** Zr vs Y/Ho diagram. **c** La_N/Sm_N vs La_N/Yb_N diagram. **d** P_2O_5 vs REY diagram. The Meishucun section data were obtained from Liu and Zhou (2017), apatite data in deep sea muds are from Liao et al. (2019), ZK2204 data are from Xu et al. (2019), carbonate and ZK2802 data are from Yang et al. (2021b), GZW section and ZK2504 data are from Xing et al. (2021), and some of the MTC data come from Wu et al. (2022).

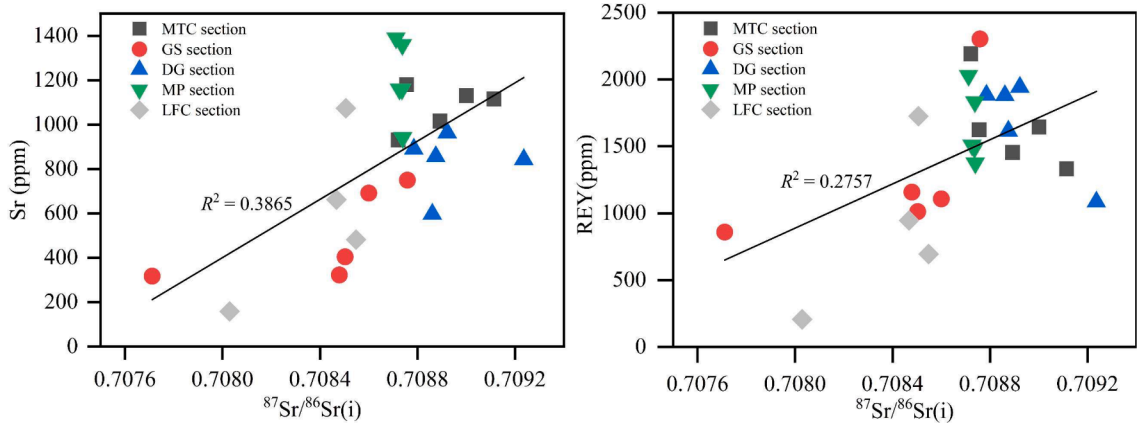

Fig. 7. Plots of $^{87}Sr/^{86}Sr(i)$ against Sr and REY contents in Zhijin phosphorites. LFC-section-data points are from Liu and Zhou (2020).

were greater than that of Na_2O, the CaO* values were equal to the Na_2O values (McLennan et al., 1993). The CIA was typically defined by CIA = (Al_2O_3 / (Al_2O_3 + CaO* + Na_2O + K_2O)) × 100 (Nesbitt and Young, 1982; Young, 2002). CIA categories included incipient (CIA = 50–60), intermediate (CIA = 60–80), and extreme (CIA > 80) chemical weathering (Fedo et al., 1995). Furthermore, the REY-rich shale is closely related to the presence of apatite in the sample, which contains REY, P_2O_5, and CaO content of 897 ppm, 22.5 %, and 30.4 %, respectively (Table 2). Its contents of Al_2O_3 and SiO_2 are comparable to that of other shales with low REY content (average 185 ppm) (Table 2). Therefore, Zhijin shales could be used to determine the influence of source rock weathering on the REY composition of Zhijin paleo-seawater, although the sedimentary facies of Zhijin shales is different from that of Zhijin phosphorites. The CIA values of Zhijin shales range from 68 to 75; meanwhile, Zhijin shales locate on the trend line of granite weathering (Fig. 8b) (Li et al., 2003; Liu et al., 2019; Huang et al., 2021). These results indicate that relatively strong granite weathering may have played an important role during the early Cambrian.

In addition, trace elements in marine chemical sediment rocks, such as Zr, can record the signal of terrestrial clasts (Webb and Kamber, 2000). There is a significant negative correlation between the Y/Ho ratios and Zr contents in Zhijin phosphorites from our investigated

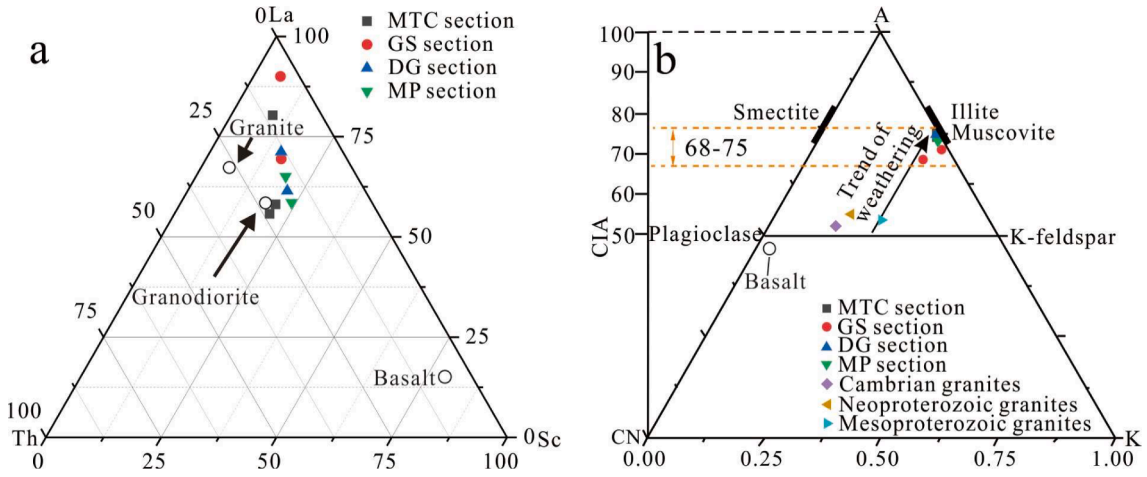

Fig. 8. Provenance of material in Zhijin paleo-seawater. **a** La-Th-Sc ternary diagram was based on Cullers and Podkovyrov (2000). **b** Ternary diagram of A-CN-K based on the method described by Nesbitt and Young (1984). The granite data are taken from Li et al. (2003), Liu et al. (2019), and Huang et al. (2021).

Table 3
Sr isotope compositions of Zhijin phosphorites.

Sample	Age (Ma)	Rb (ppm)	Sr (ppm)	Mn (ppm)	$^{87}Rb/^{86}Sr$	$^{87}Sr/^{86}Sr$	2SE	$^{87}Sr/^{86}Sr(i)$	Mn/Sr
MTC-1	542	21.7	1115	547	0.056315	0.709549	0.000010	0.709114	0.49
MTC-2	542	24.2	930	261	0.075296	0.709303	0.000008	0.708721	0.28
MTC-3	542	27	1130	204	0.069139	0.709535	0.000010	0.709001	0.18
MTC-4	542	3.1	1180	119	0.007602	0.708814	0.000007	0.708755	0.10
MTC-5	542	5.2	1015	53	0.014824	0.709007	0.000008	0.708892	0.05
GS-1	542	39.1	323	99	0.350277	0.711185	0.000006	0.708479	0.31
GS-2	542	27.2	692	233	0.113736	0.709479	0.000005	0.708600	0.34
GS-3	542	19.9	405	139	0.142179	0.709601	0.000006	0.708503	0.34
GS-4	542	8	750	146	0.030865	0.708996	0.000006	0.708758	0.19
GS-5	542	50.9	318	189	0.463156	0.711289	0.000008	0.707711	0.59
DG-1	542	15.8	843	237	0.054233	0.709655	0.000007	0.709236	0.28
DG-2	542	26	597	277	0.126019	0.709835	0.000007	0.708861	0.46
DG-3	542	17	963	76	0.051081	0.709317	0.000007	0.708922	0.08
DG-4	542	5.6	856	69	0.018930	0.709021	0.000008	0.708875	0.08
DG-5	542	1.6	890	92	0.005202	0.708825	0.000012	0.708785	0.10
MP-1	542	15	941	38	0.046125	0.709095	0.000006	0.708739	0.04
MP-2	542	6.2	1390	92	0.012907	0.708812	0.000006	0.708712	0.07
MP-3	542	4.3	1160	419	0.010726	0.708809	0.000011	0.708726	0.36
MP-4	542	7.1	1360	144	0.015106	0.708855	0.000006	0.708738	0.11
MP-5	542	6.7	1160	84	0.016713	0.708865	0.000006	0.708736	0.07

Table 4
Nd isotope compositions of Zhijin phosphorites.

Samples	Age(Ma)	Sm(ppm)	Nd(ppm)	$^{147}Sm/^{144}Nd$	$^{143}Nd/^{144}Nd$	2SE	$^{143}Nd/^{144}Ndi$	$\varepsilon_{Nd}(t)$	T_{2DM} (Ga)
MTC-1	542	41.0	217	0.1142	0.511997	0.000002	0.511591593	−6.8	1.8
MTC-2	542	72.1	386	0.1129	0.511980	0.000001	0.511579212	−7.0	1.8
MTC-3	542	46.8	257	0.1100	0.511983	0.000002	0.511592267	−6.8	1.8
MTC-4	542	42.0	235	0.1080	0.511954	0.000002	0.511570515	−7.2	1.8
MTC-5	542	41.6	230	0.1093	0.511953	0.000001	0.51156491	−7.3	1.9
GS-1	542	28.8	139	0.1254	0.511965	0.000001	0.511519785	−8.2	1.9
GS-2	542	32.8	147	0.1350	0.511988	0.000001	0.511508581	−8.4	1.9
GS-3	542	66.3	345	0.1161	0.511976	0.000001	0.511563654	−7.3	1.9
GS-4	542	26.4	127	0.1261	0.512016	0.000001	0.511568204	−7.3	1.9
DG-1	542	32.6	161	0.1224	0.511998	0.000001	0.511563531	−7.3	1.9
DG-2	542	67.7	302	0.1355	0.511978	0.000001	0.511496996	−8.6	2.0
DG-3	542	60.4	309	0.1181	0.511991	0.000001	0.511571583	−7.2	1.8
DG-4	542	46.9	236	0.1201	0.511950	0.000002	0.511523589	−8.1	1.9
DG-5	542	54.8	266	0.1245	0.511976	0.000001	0.511533955	−7.9	1.9
MP-1	542	38.8	208	0.1127	0.511962	0.000002	0.511561746	−7.4	1.9
MP-2	542	62.0	334	0.1122	0.511968	0.000002	0.511569698	−7.2	1.8
MP-3	542	45.1	247	0.1103	0.511962	0.000001	0.511570216	−7.2	1.8
MP-4	542	53.7	295	0.1100	0.511966	0.000002	0.511575411	−7.1	1.8
MP-5	542	46.3	248	0.1128	0.511977	0.000002	0.511576413	−7.1	1.8

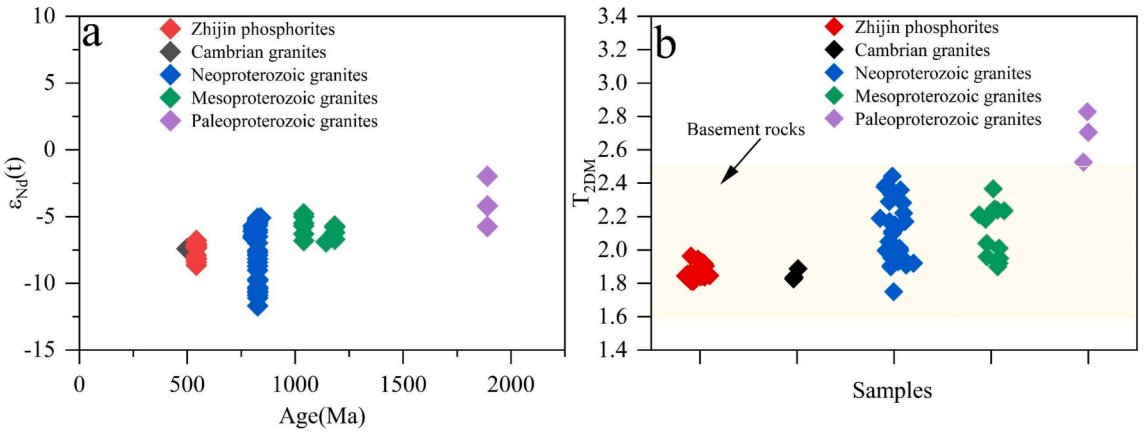

Fig. 9. Identification of the relationship between REY source and granite. **a** The Nd isotopes ($\varepsilon_{Nd}(t)$) distribution of Zhijin phosphorites and granites of different ages. **b** Two-stage Nd model ages (T_{2DM}) signature of Zhijin phosphorites and granites of different ages. Cambrian granite data are from Shen et al. (2000). Neoproterozoic granite data are from Li et al. (2003), Zhao et al. (2013), Huang et al. (2019), and Zhu et al. (2019). Mesoproterozoic granite data are from Zhu et al. (2020) and Huang et al. (2021). Paleoproterozoic granite data are from Shen et al. (2000). Basement rock data are from Zhang and Zheng (2013).

sections, but no correlation is observed in contemporaneous Meishucun phosphorites (Fig. 6b) (Liu and Zhou, 2017; Wu et al., 2022). With a decrease in the Y/Ho ratios of Zhijin phosphorites, Sm_N/Yb_N ratios also increase gradually (Fig. 6a) (Xing et al., 2021; Wu et al., 2022), suggesting that terrigenous supplies led to the REY pattern of HREE depletion. The contemporaneous Meishucun phosphorites without REY enrichment mainly fall above the seawater line; however, Zhijin phosphorites gradually approach the terrigenous line (Fig. 6a) (Liu and Zhou, 2017; Xing et al., 2021; Wu et al., 2022), suggesting that REY enrichment was associated with terrestrial supply. On the other hand, the average REY content of carbonates in Zhijin phosphorites is 51.4 ppm, which is greater than the average REY content (3.78 ppm) of dolomites in contemporaneous Meishucun phosphorites (Liang et al., 2018; Yang et al., 2021b). Meanwhile, black shales have an average REY content of 185 ppm at the top of Gezhongwu Formation, which is much larger than those of dolomites (as low as 5.72 ppm) at the top of contemporaneous Meishucun Formation (Liu and Zhou, 2017). This indicates a higher REY background value in Zhijin seawater. Zhijin phosphorites exhibit a positive correlation between P_2O_5 and REY contents (Fig. 6d) (Xu et al., 2019; Xing et al., 2021; Yang et al., 2021b; Wu et al., 2022). Interestingly, phosphorites at the bottom of MTC and GS sections have low REY contents, and a sharp increase in REY content occurred during phosphorus deposition (Fig. 6d) (Wu et al., 2022), indicating that the phosphorus source was inconsistent with the REY source. The Y/Ho values of carbonates in Zhijin phosphorites range from 35 to 61 (Yang et al., 2021b), and it is clear that the Y/Ho values were influenced by terrestrial materials (Fig. 6a). The Er/Nd ratio for typical seawater is approximately 0.27 (de Baar et al., 1988). It is <0.1 due to the preferential enrichment of Nd compared to Er under the combined influence of clastic materials and diagenesis (German and Elderfield, 1990; Bellanca et al., 1997). The Er/Nd ratios in Zhijin phosphorites range from 0.09 to 0.13, suggesting the importance of terrestrial supplies.

5.2.2. Nd isotopes

The assembly of Gondwanaland allowed for enhanced continental weathering, which resulted in a large number of terrestrial materials being transported into the ocean (Peters and Gaines, 2012). The very low $\varepsilon_{Nd}(t)$ value of early Cambrian seawater also confirmed the high continental weathering at that time (Keto and Jacobsen, 1988; Maloof et al., 2010; Peters and Gaines, 2012). It has also been suggested that the Sm-Nd isotope system played an important role in the study of sedimentary provenance (O'nions et al., 1983; Allègre and Rousseau, 1984; Goldstein and Jacobsen, 1988; Miller and Harris, 1989; Zhao et al., 1992). It was not significantly disturbed during sedimentation or diagenesis, which makes it possible to determine the provenance's mean crustal age (McCulloch and Wasserburg, 1978). The negative $\varepsilon_{Nd}(t)$ values (−8.6 to −6.8) of Zhijin phosphorites in this study (Fig. 9a) and previous $\varepsilon_{Nd}(t)$ values (−12 to −10 and −7.0 to −6.1) of Zhijin phosphorites analyzed by Liu and Zhou (2020) and Zhang et al. (2021), indicate that continental crust was a key REY source.

The upper continental crust is mainly composed of granodioritic bulk (Wedepohl, 1995), and granite was an important material source of Zhijin sediment. The mean $\varepsilon_{Nd}(t)$ values and T_{2DM} of granites in South China are −7.2 and 1.6 Ga, respectively (Hong et al., 1998). The low $\varepsilon_{Nd}(t)$ values require a LREY-enriched supply, as would be expected for rocks originating from the continental crust. Therefore, based on the negative $\varepsilon_{Nd}(t)$ values, the material sources of granites from South China were mainly derived from the recycling of ancient crusts. The mean T_{2DM} from South China is consistent with the ages of the Paleoproterozoic basement rocks, ranging from 1.6 to 2.5 Ga (Zhang and Zheng, 2013), indicating that the bulk of South China originated from the partial melting of Paleoproterozoic crust. The $\varepsilon_{Nd}(t)$ values (from −8.6 to −6.8) and T_{2DM} (from 1.8 to 2.0 Ga) of Zhijin phosphorites are consistent with those of most granites in South China, suggesting that REY in Zhijin phosphorites might be primarily derived from Paleoproterozoic crust recycling. During the early Cambrian, some granitoid rocks with $\varepsilon_{Nd}(t)$ values of approximately −8 potentially existed in the continental crust of South China, and many granitoid rocks were likely weathered to seawater. This is supported by the distribution of a few Cambrian granites with $\varepsilon_{Nd}(t)$ values of approximately −8 and T_{2DM} values of 1.8 Ga, which is consistent with the age of Paleoproterozoic basement rocks (Fig. 9) (Shen et al., 2000; Zhang and Zheng, 2013).

Except for Cambrian granites, the Proterozoic granites may also be weathered to shallow seawater. Studies have observed Neoproterozoic granites with $\varepsilon_{Nd}(t)$ values ranging from −5.1 to −11.7 and T_{2DM} ranging from 1.8 to 2.4 Ga (Paleoproterozoic) (Li et al., 2003; Zhao et al., 2013; Huang et al., 2019; Zhu et al., 2019). The $\varepsilon_{Nd}(t)$ values and T_{2DM} of Mesoproterozoic granites range from −6.9 to −4.8, from 1.9 to 2.4 Ga (Paleoproterozoic), respectively (Zhu et al., 2020; Huang et al., 2021). However, the $\varepsilon_{Nd}(t)$ values and T_{2DM} of Paleoproterozoic granites range from −5.8 to −2.0, from 2.5 to 2.8 Ga (Archeozoic), respectively (Shen et al., 2000). Interestingly, T_{2DM} (1.8–2.0 Ga) of Zhijin phosphorites is consistent with the major Phanerozoic, Neoproterozoic, and Mesoproterozoic granites (Fig. 9b) (Hong et al., 1998; Shen et al., 2000; Li et al., 2003; Zhao et al., 2013; Huang et al., 2019; Zhu et al., 2019; Zhu et al., 2020; Huang et al., 2021). Meanwhile, the $\varepsilon_{Nd}(t)$ values of Zhijin phosphorites are consistent with those of the Cambrian, Mesoproterozoic, and Neoproterozoic granites (Fig. 9a) (Shen et al., 2000; Li et al., 2003; Zhao et al., 2013; Huang et al., 2019; Zhu et al., 2019; Zhu et al., 2020; Huang et al., 2021). Therefore, Mesoproterozoic and

Neoproterozoic granites should be considered together when considering Cambrian granites weathering. The La_N/Yb_N and Gd_N/Yb_N ratios and Yb_N/Nd_N-$\varepsilon_{Nd}(t)$ scatter diagrams can also discriminate sediment sources (Van De Flierdt et al., 2012; Filippova et al., 2017; Cao et al., 2019; Casse et al., 2019). Granite weathering resulted in a gradual increase in La_N/Yb_N and Gd_N/Yb_N ratios, and the La_N/Yb_N and Gd_N/Yb_N ratios of Zhijin phosphorites are similar to those of weathering granites and detrital sediments (Fig. 10a) (Li et al., 2003; Cao et al., 2019; Casse et al., 2019; Liu et al., 2019; Liu and Zhou, 2020; Li et al., 2020; Huang et al., 2021; Wu et al., 2022). In addition, the Yb_N/Nd_N-$\varepsilon_{Nd}(t)$ scatter diagram also exhibits that the samples of Zhijin phosphorites are located near the clastic line (Fig. 10b) (Van De Flierdt et al., 2012; Filippova et al., 2017; Cao et al., 2019; Casse et al., 2019; Liu and Zhou, 2020). Therefore, the weathering of granites may provide dominant REY sources to Zhijin phosphorites.

5.3. REY migrating into ocean by granite weathering

PAAS-normalized REY patterns from Cambrian, Mesoproterozoic, and Neoproterozoic fresh granites exhibit slight HREY enrichment (Fig. 4a) (Li et al., 2003; Liu et al., 2019; Huang et al., 2021). A previous study has suggested that granite hillslope processes can result in REY redistribution (Li et al., 2020). Variations in slope unevenness can cause differences in the slope process intensity, such as runoff erosion, creep, and landslides (Li et al., 2020). If denudation is severe in an uphill environment, the downhill migration of REY can be significant and is related to surface runoff, subsurface flow, and groundwater flow (Braun et al., 2017; Braun et al., 2018). During the early Cambrian period, extensive orogenic movement together with the Gondwana supercontinent aggregation caused significant topographical differences (Wei et al., 2019), which may have led to a large number of granites being exposed to the surface, thereby enhancing continental denudation. The existence of a paleo-weathering crust at the bottom of Gezhongwu Formation in the MTC section also indicates strong continental weathering (Fig. 3i). The illite has poor roundness as a terrigenous clastic mineral (Fig. 3n, o), indicating that the transport distance of source rock was relatively small during continental weathering.

In hillslope processes, active exposure provided sufficient fresh feldspar and biotite from granite to form kaolinite and halloysite. At the ridgetop, LREY was preferentially adsorbed onto clay minerals through outer-sphere complexation (Galán et al., 2007; Sanematsu et al., 2013), resulting in REY pattern of HREY depletion and negative Ce anomaly in the ridgetop profile (Fig. 4c) (Li et al., 2020). HREY was transported to groundwater due to stable HREY-carbonate complex compounds in soil solutions (Wood, 1990; Lee and Byrne, 1993; Li et al., 2019), resulting in the gradual enrichment of HREY in the upslope and footslope profiles compared to the bedrock (Fig. 4c) (Li et al., 2020). After granite hillslope processes occurred, REY contents are more enriched in the ridgetop than in the footslope profile (Li et al., 2020). Meanwhile, the HREY contents are more than three times higher in the ridgetop profile (average 201 ppm, n = 7) than in the bedrock (average 48.9 ppm, n = 10) (Fig. 4c) (Li et al., 2020); this resulted in the formation of regolith-hosted REY deposits at the ridgetop (Fig. 11a) (Li et al., 2020). Given the intense erosion facilitated chemical weathering during the early Cambrian, the regolith-hosted REY was transported into Zhijin seawater, resulting in REY enrichment in Zhijin phosphorites (Fig. 11b). Therefore, it is reasonable that the terrigenous supply of REY resulted in the transformation of HREY depletion in Zhijin phosphorites.

6. Conclusion

Zhijin phosphorite exhibits a REY pattern with HREY depletion and negative Ce anomaly. On the one hand, the La_N/Sm_N-La_N/Yb_N diagram, Y/Ho ratios, and Sr isotopes of Zhijin phosphorites evidence a partial contribution of seawater-sourced REY. On the other hand, the La-Th-Sc and A-CN-K diagrams of Zhijin shales indicate that granite weathering had an important influence on the chemical composition of Zhijin paleo-seawater. The $^{87}Sr/^{86}Sr(i)$ values of Zhijin phosphorites exhibit positive correlations with their Sr and REY contents, and their Y/Ho ratios exhibit negative correlations with Zr contents and Sm_N/Yb_N ratios, which also indicate that REY was primarily derived from terrigenous material. Meanwhile, this also caused a REY pattern of HREY depletion in Zhijin paleo-seawater.

Furthermore, the $\varepsilon_{Nd}(t)$ values (from −8.6 to −6.8) and T_{2DM} (from 1.8 to 2.0 Ga) of Zhijin phosphorites are consistent with those of most granites in South China, suggesting that REY in Zhijin phosphorites was primarily derived from partial melting of the Paleoproterozoic crust. Finally, the regolith-hosted REY formed by granite weathering was transported to Zhijin seawater, resulting in REY enrichment in Zhijin phosphorites. Granite weathering, such as the Mesozoic ion adsorption-type REY deposits from South China, could be a common phenomenon during geological history. Overall, this study provides a new perspective on the relationship between granite weathering and marine REY deposition, although more evidence is needed to support this model.

Declaration of Competing Interest

The authors declare that they have no known competing financial interests or personal relationships that could have appeared to influence the work reported in this paper.

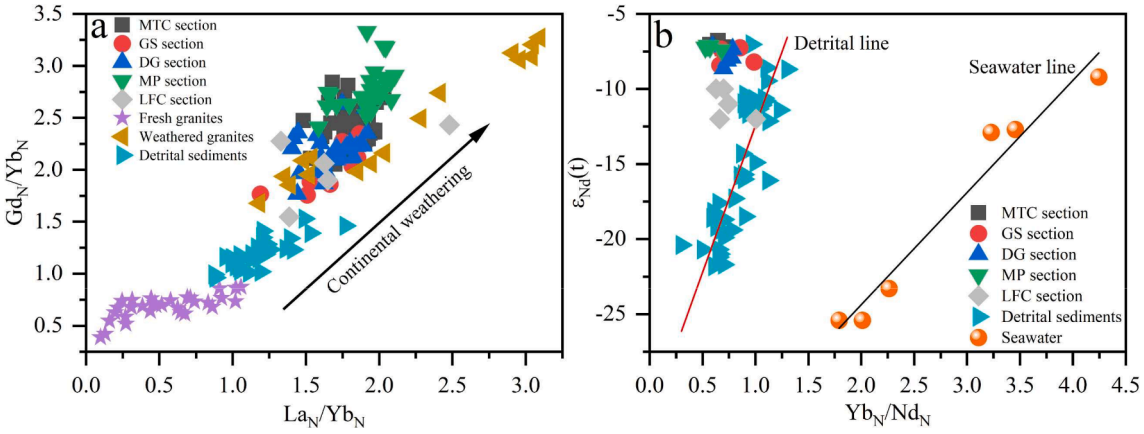

Fig. 10. Scatter diagrams about continental weathering source of Zhijin phosphorites. **a** La_N/Yb_N vs Gd_N/Yb_N. **b** Yb_N/Nd_N vs $\varepsilon_{Nd}(t)$ diagram including detrital sediment and seawater samples. LFC section data are from Liu and Zhou (2020). Fresh granite data are from Li et al. (2003), Liu et al. (2019), and Huang et al. (2021). Weathered granite data are from Li et al. (2020). Detrital sediment data are from Casse et al. (2019) and Cao et al. (2019). Seawater data are from Van De Flierdt et al. (2012) and Filippova et al. (2017). Some of the MTC data come from Wu et al. (2022).

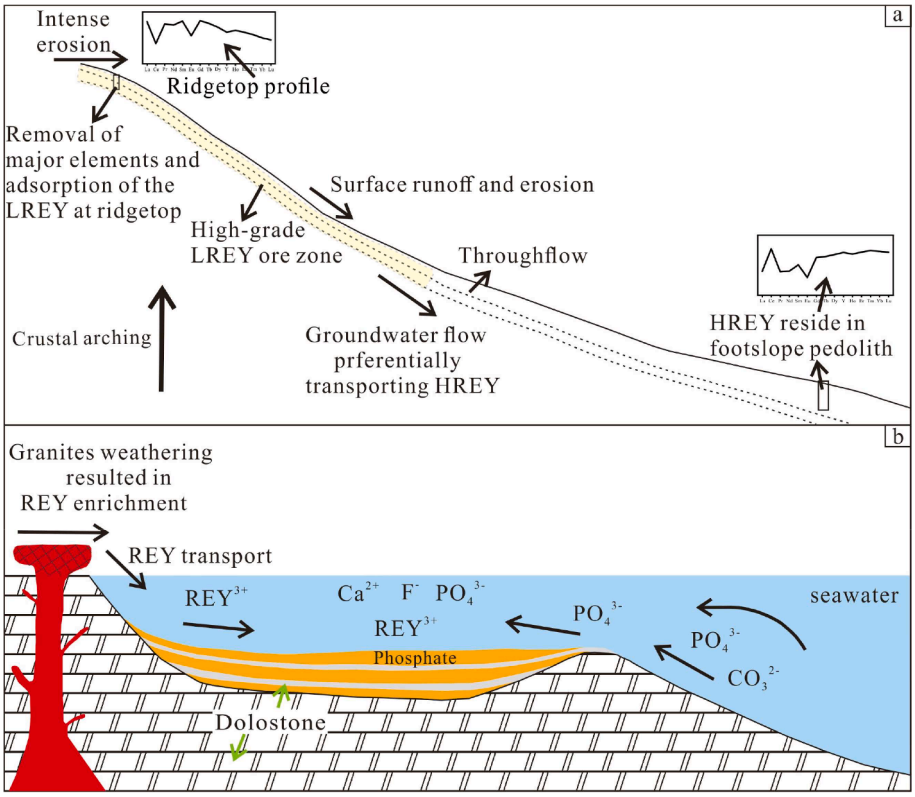

Fig. 11. Diagram of REY enrichment in Zhijin phosphorites from early Cambrian in Guizhou, China. The granite hillslope process was modified from Li et al. (2020).

Data availability

Data will be made available on request.

Acknowledgments

This research was supported by the National Natural Science Foundation of China (92062221, U1812402, 41890840, 4207030265, 42121003, 41773015), CAS IIT (JCTD-2019-17), Guizhou Provincial 2020 Science and Technology Subsidies (GZ2020SIG), and Key R&D Program of Yunnan Province (202103AQ100003). We sincerely thank the engineers, namely, Fang Xiao and Xiaobiao Li, at the State Key Laboratory of Ore Deposit Geochemistry, Chinese Academy of Sciences, for their help with the requisite experiments. We would like to thank Dr. Zhuojun Xie from the Institute of Geochemistry, Chinese Academy of Sciences, for his suggestions on this article.

Appendix A. Supplementary data

Supplementary data to this article can be found online at https://doi.org/10.1016/j.oregeorev.2022.105146.

References

Abedini, A., Calagari, A.A., 2017. REEs geochemical characteristics of lower Cambrian phosphatic rocks in the Gorgan-Rasht Zone, northern Iran: Implications for diagenetic effects and depositional conditions. J. Afr. Earth Sci. 135, 115–124.

Allègre, C.J., Rousseau, D., 1984. The growth of the continent through geological time studied by Nd isotope analysis of shales. Earth Planet Sci. Lett. 67 (1), 19–34.

Bau, M., Dulski, P., 1996. Distribution of yttrium and rare-earth elements in the Penge and Kuruman iron-formations, Transvaal Supergroup, South Africa. Precambrian Research 79 (1-2), 37–55.

Bau, M., Möller, P., Dulski, P., 1997. Yttrium and lanthanides in eastern Mediterranean seawater and their fractionation during redox-cycling. Mar. Chem. 56 (1-2), 123–131.

Bellanca, A., Masetti, D., Neri, R., 1997. Rare earth elements in limestone/marlstone couplets from the Albian-Cenomanian Cismon section (Venetian region, northern Italy): assessing REE sensitivity to environmental changes. Chem. Geol. 141 (3-4), 141–152.

Bhatia, M.R., Crook, K.A.W., 1986. Trace element characteristics of graywackes and tectonic setting discrimination of sedimentary basins. Contrib. to Mineral Petrol. 92 (2), 181–193.

Borst, A.M., Smith, M.P., Finch, A.A., Estrade, G., Villanova-de-Benavent, C., Nason, P., Marquis, E., Horsburgh, N.J., Goodenough, K.M., Xu, C., Kynicky, J., Geraki, K., 2020. Adsorption of rare earth elements in regolith-hosted clay deposits. Nat. Commun. 11, 4386.

Braun, J.-J., Riotte, J., Battacharya, S., Violette, A., Prunier, J., Bouvier, V., Candaudap, F., Maréchal, J.-C., Ruiz, L., Panda, S.R., Subramanian, S., 2017. REY-Th-U solute dynamics in the critical zone: Combined influence of chemical weathering, atmospheric deposit leaching, and vegetation cycling (Mule Hole Watershed, South India). Geochem. Geophys. 18 (12), 4409–4425.

Braun, J.-J., Riotte, J., Battacharya, S., Violette, A., Oliva, P., Prunier, J., Maréchal, J.-C., Ruiz, L., Audry, S., Subramanian, S., 2018. REY-Th-U dynamics in the critical zone: Combined influence of reactive bedrock accessory minerals, authigenic phases, and hydrological sorting (Mule Hole Watershed, South India). Geochem. Geophys. 19 (5), 1611–1635.

Cao, L., Liu, J., Shi, X., He, W., Chen, Z., 2019. Source-to-sink processes of fluvial sediments in the northern South China Sea: Constraints from river sediments in the coastal region of South China. J. Asian Earth Sci. 185, 104020.

Casse, M., Montero-Serrano, J.-C., St-Onge, G., Poirier, A., 2019. REE distribution and Nd isotope composition of estuarine waters and bulk sediment leachates tracing lithogenic inputs in eastern Canada. Mar. Chem. 211, 117–130.

Chen, F., Cui, X., Lin, S., Wang, J., Yang, X., Ren, G., Pang, W., 2021. The 1.14 Ga mafic intrusions in the SW Yangtze Block, South China: Records of late Mesoproterozoic intraplate magmatism. J. Asian Earth Sci. 205.

Chen, Y.-Q., Jiang, S.-Y., Ling, H.-F., Yang, J.-H., 2009. Pb–Pb dating of black shales from the Lower Cambrian and Neoproterozoic strata, South China. Geochemistry 69 (2), 183–189.

Cullers, R.L., 1994. The controls on the major and trace element variation of shales, siltstones, and sandstones of Pennsylvanian-Permian age from uplifted continental blocks in Colorado to platform sediment in Kansas, USA. Geochim. Cosmochim. Acta 58 (22), 4955–4972.

Cullers, R.L., Podkovyrov, V.N., 2000. Geochemistry of the Mesoproterozoic Lakhanda shales in southeastern Yakutia, Russia: implications for mineralogical and provenance control, and recycling. Precambrian Res. 104, 77–93.

de Baar, H.J.W., German, C.R., Elderfield, H., van Gaans, P., 1988. Rare earth element distributions in anoxic waters of the Cariaco Trench. Geochim. Cosmochim. Acta 52 (5), 1203–1219.

Derry, L.A., Brasier, M.D., Corfield, R.M., Rozanov, A.Y., Zhuravlev, A.Y., 1994. Sr and C isotopes in Lower Cambrian carbonates from the Siberian craton: a paleoenvironmental record during the 'Cambrian explosion'. Earth & Planet Sci. Lett. 128 (3-4), 671–681.

Edmond, J.M., 1992. Himalayan tectonics, weathering processes, and the strontium isotope record in marine limestones. Science 258 (5088), 1594–1597.
Emsbo, P., McLaughlin, P.I., Breit, G.N., du Bray, E.A., Koenig, A.E., 2015. Rare earth elements in sedimentary phosphate deposits: Solution to the global REE crisis? Gondwana Res. 27 (2), 776–785.
Fathin, K.P.F., Gireeshkumar, T.R., Furtado, C.M., Cyriac, M., Arya, K.S., Shaik, A., Paul, J., Vignesh, E.R., Balachandran, K.K., 2021. Phosphorus cycling from a coastal upwelling zone in the Southeastern Arabian Sea. Environmental Monitoring and Assessment 193, 188.
Fedo, C.M., Wayne Nesbitt, H., Young, G.M., 1995. Unraveling the effects of potassium metasomatism in sedimentary rocks and paleosols, with implications for paleoweathering conditions and provenance. Geology 23, 921–924.
Filippova, A., Frank, M., Kienast, M., Rickli, J., Hathorne, E., Yashayaev, I.M., Pahnke, K., 2017. Water mass circulation and weathering inputs in the Labrador Sea based on coupled Hf–Nd isotope compositions and rare earth element distributions. Geochim. Cosmochim. Acta 199, 164–184.
Gadd, M.G., Layton-Matthews, D., Peter, J.M., 2016. Non-hydrothermal origin of apatite in SEDEX mineralization and host rocks of the Howard's Pass district, Yukon. Canada. Am. Mineral 101 (5), 1061–1071.
Galán, E., Fernández-Caliani, J.C., Miras, A., Aparicio, P., Márquez, M.G., 2007. Residence and fractionation of rare earth elements during kaolinization of alkaline peraluminous granites in NW Spain. Clay Miner. 42 (3), 341–352.
Garnit, H., Bouhlel, S., Barca, D., Chtara, C., 2012. Application of LA-ICP-MS to sedimentary phosphatic particles from Tunisian phosphorite deposits: Insights from trace elements and REE into paleo-depositional environments. Chem. Erde-Geochem. 72 (2), 127–139.
German, C.R., Elderfield, H., 1990. Application of the Ce anomaly as a paleoredox indicator: The ground rules. Paleoceanography 5 (5), 823–833.
Glenn, C.R., Follmi, K.B., Riggs, S.R., Baturin, G.N., Grimm, K.A., Trappe, J., Abed, A.M., Galliolivier, C., Garrison, R.E., Ilyin, A.V., Jehl, C., Rohrlich, V., Sadaqah, R.M.Y., Schidlowski, M., Sheldon, R.E., Siegmund, H., 1994. Phosphorus and Phosphorites: Sedimentology and Environments of Formation. Eclogae Geologicae Helvetiae 87, 747–788.
Goldstein, S.J., Jacobsen, S.B., 1988. Nd and Sr isotopic systematics of river water suspended material: implications for crustal evolution. Earth & Planet Sci. Lett. 87 (3), 249–265.
Gong, X., Wu, S., Xia, Y., Zhang, Z., He, S., Xie, Z., Xiao, J., Yang, H., Tan, Q., Huang, Y.i., Yang, Y., 2021. Enrichment characteristics and sources of the critical metal yttrium in Zhijin rare earth-containing phosphorites, Guizhou Province. China. Acta. Geochim. 40 (3), 441–465.
Grandjean-Lécuyer, P., Feist, R., Albarède, F., 1993. Rare earth elements in old biogenic apatites. Geochimica et Cosmochimica Acta 57 (11), 2507–2514.
Haley, B.A., Klinkhammer, G.P., McManus, J., 2004. Rare earth elements in pore waters of marine sediments. Geochimica et Cosmochimica Acta 68 (6), 1265–1279.
Halverson, G.P., Dudás, F.Ö., Maloof, A.C., Bowring, S.A., 2007. Evolution of the 87Sr/86Sr composition of Neoproterozoic seawater. Palaeogeogr. Palaeoclimatol. Palaeoecol. 256 (3-4), 103–129.
Hannigan, R.E., Sholkovitz, E.R., 2001. The development of middle rare earth element enrichments in freshwaters: weathering of phosphate minerals. Chem. Geol. 175 (3-4), 495–508.
Hong, D., Xie, X., Zhang, J., 1998. Isotope geochemistry of granitoids in South China and their metallogeny. Resour. Geol. 48, 251–263.
Huang, M., Cui, X., Lin, S., Chen, J., Ren, G., Sun, Z., Ren, F., Xu, Q., 2021. The ca. 1.18–1.14 Ga A-type granites in the southwestern Yangtze Block, South China: New evidence for late Mesoproterozoic continental rifting. Precambrian Res. 363, 106358.
Huang, S-F., Wang, W., Pandit, M.K., Zhao, J-H., Lu, G-M., Xue, E-K., 2019. Neoproterozoic S-type granites in the western Jiangnan Orogenic Belt, South China: Implications for petrogenesis and geodynamic significance. Lithos 342, 45-58.
Humphries, M., 2012. Rare Earth Elements: The Global Supply Chain.
Ingram, B.L., 1995. High-resolution dating of deep-sea clays using Sr isotopes in fossil fish teeth. Earth & Planet Sci. Lett. 134 (3-4), 545–555.
Ingram, B.L., Coccioni, R., Montanari, A., Richter, F.M., 1994. Strontium isotopic composition of mid-Cretaceous seawater. Science 264 (5158), 546–550.
Jacobsen, S.B., Kaufman, A.J., 1999. The Sr, C and O isotopic evolution of Neoproterozoic seawater. Chemical Geology 161, 37–57.
Jarvis, I., Burnett, W.C., Nathan, Y., Almbaydin, F.S.M., Attia, A.K.M., Castro, L.N., Flicoteaux, R., Hilmy, M.E., Husain, V., Qutawnah, A.A., Serjani, A., Zanin, Y.N., 1994. Phosphorite geochemistry - state-of-the-art and environmental concerns. Eclogae Geol. Helv. 87, 643–700.
Jiang, S.Y., Zhao, H.X., Chen, Y.Q., Yang, T., Yang, J.H., Ling, H.F., 2007. Trace and rare earth element geochemistry of phosphate nodules from the lower Cambrian black shale sequence in the Mufu Mountain of Nanjing, Jiangsu province, China. Chemical Geology 244, 584–604.
Joosu, L., Lepland, A., Kirsimäe, K., Romashkin, A.E., Roberts, N.M., Martin, A.P., Črne, A.E., 2015. The REE-composition and petrography of apatite in 2 Ga Zaonega Formation, Russia: The environmental setting for phosphogenesis. Chem. Geol. 395, 88–107.
Kaufman, A.J., Knoll, A.H., 1995. Neoproterozoic variations in the C-isotopic composition of seawater: stratigraphic and biogeochemical implications. Precambrian research 73, 27–49.
Keto, L.S., Jacobsen, S.B., 1988. Nd isotopic variations of Phanerozoic paleoceans. Earth & Planet Sci. Lett. 90, 395–410.
Kidder, D.L., Eddy, C.A., 1994. Rare-earth element variation in phosphate nodules from midcontinent Pennsylvanian cyclothems. Journal of Sedimentary Research - Section A; (United States) 64, 584–592.
Kon, Y., Hoshino, M., Sanematsu, K., Morita, S., Tsunematsu, M., Okamoto, N., Yano, N., Tanaka, M., Takagi, T., 2014. Geochemical Characteristics of Apatite in Heavy REE-rich Deep-Sea Mud from Minami-Torishima Area, Southeastern Japan. Resour. Geol. 64, 47–57.
Kuznetsov, A., Semikhatov, M., Gorokhov, I., 2018. Strontium isotope stratigraphy: principles and state of the art. Stratigr. Geol. Correl. 26, 367–386.
Kynicky, J., Smith, M.P., Xu, C., 2012. Diversity of Rare Earth Deposits: The Key Example of China. Elements 8, 361–367.
Lécuyer, C., Reynard, B., Grandjean, P., 2004. Rare earth element evolution of Phanerozoic seawater recorded in biogenic apatites. Chem. Geol. 204, 63–102.
Lee, J.H., Byrne, R.H., 1993. Complexation of trivalent rare earth elements (Ce, Eu, Gd, Tb, Yb) by carbonate ions. Geochim. Cosmochim. Acta 57, 295–302.
Lehmann, A., Myrberg, K., 2008. Upwelling in the Baltic Sea — A review. Journal of Marine Systems 74, S3–S12.
Li, Z.X., Evans, D.A., Halverson, G.P., 2013. Neoproterozoic glaciations in a revised global palaeogeography from the breakup of Rodinia to the assembly of Gondwanaland. Sediment Geol. 294, 219–232.
Li, X.-H., Li, Z.-X., Ge, W., Zhou, H., Li, W., Liu, Y., Wingate, M.T., 2003. Neoproterozoic granitoids in South China: crustal melting above a mantle plume at ca. 825 Ma? Precambrian Res. 122, 45–83.
Li, C., Li, X., Li, Q., Guo, J., Yang, Y., 2012. Rapid and precise determination of Sr and Nd isotopic ratios in geological samples from the same filament loading by thermal ionization mass spectrometry employing a single-step separation scheme. Analytica. Chimica. Acta 727, 54–60.
Li, C., Ripley, E.M., Tao, Y., Hu, R., 2016. The significance of PGE variations with Sr–Nd isotopes and lithophile elements in the Emeishan flood basalt province from SW China to northern Vietnam. Lithos 248, 1–11.
Li, M.Y.H., Zhou, M.F., Williams-Jones, A.E., 2019. The genesis of regolith-hosted heavy rare earth element deposits: Insights from the world-class Zudong deposit in Jiangxi Province, South China. Econ. Geol. 114, 541–568.
Li, M.Y.H., Zhou, M.F., Williams-Jones, A.E., 2020. Controls on the Dynamics of Rare Earth Elements During Subtropical Hillslope Processes and Formation of Regolith-Hosted Deposits. Econ. Geol. 115, 1097–1118.
Liang, Y.-Z., Su, Y.-Y., Su, X.-Z., Chi, H.-T., 2018. Modes of occurrence of rare earth elements in Kunyang phosphorite deposit. Yunnan Province. Acta Petrol. Mineral. 37, 959–966 in Chinese with English abstract.
Liao, J., Sun, X., Li, D., Sa, R., Lu, Y., Lin, Z., Xu, L., Zhan, R., Pan, Y., Xu, H., 2019. New insights into nanostructure and geochemistry of bioapatite in REE-rich deep-sea sediments: LA-ICP-MS, TEM, and Z-contrast imaging studies. Chem. Geol. 512, 58–68.
Liu, X.-Q., Zhang, C.-L., Ye, X.-T., Zou, H., Hao, X.-S., 2019. Cambrian mafic and granitic intrusions in the Mazar-Tianshuihai terrane, West Kunlun Orogenic Belt: Constraints on the subduction orientation of the Proto-Tethys Ocean. Lithos 350, 105226.
Liu, X., Zhang, H., Tang, Y., Liu, Y., 2020. REE Geochemical Characteristic of Apatite: Implications for Ore Genesis of the Zhijin Phosphorite. Minerals 10, 1012.
Liu, Z.R.R., Zhou, M.F., 2017. Meishucun phosphorite succession (SW China) records redox changes of the early Cambrian ocean. GSA. Bulletin.
Liu, Z.R.R., Zhou, M.F., 2020. Early Cambrian ocean mixing recorded by phosphorite successions in the Nanhua Basin. South China. Precambrian Res. 349, 14.
Long, K.R., Van Gosen, B.S., Foley, N.K., Cordier, D., 2012. The principal rare earth elements deposits of the United States: A summary of domestic deposits and a global perspective Non-renewable resource issues. Springer 131–155.
Lou, F., Gu, S., 2020. LA-ICP-MS REE Analyses for Phosphates and Dolomites in Cambrian Phosphorite in Zhijin, Guizhou Province: Implication for Depositional Conditions and Diagenetic Processes. J. Chin. Rare Earth Soc. 38, 225–239 in Chinese with English abstract.
Ma, P., Wang, L., Wang, C., Wu, X., Wei, Y., 2015. Organic-matter accumulation of the lacustrine Lunpola oil shale, central Tibetan Plateau: Controlled by the paleoclimate, provenance, and drainage system. International Journal of Coal Geology 147–148, 58–70.
Maloof, A.C., Porter, S.M., Moore, J.L., Dudas, F.O., Bowring, S.A., Higgins, J.A., Fike, D. A., Eddy, M.P., 2010. The earliest Cambrian record of animals and ocean geochemical change. Geol. Soc. Am. Bull. 122, 1731–1774.
McArthur, J.M., Howarth, R., Bailey, T., 2001. Strontium isotope stratigraphy: LOWESS version 3: best fit to the marine Sr-isotope curve for 0–509 Ma and accompanying look-up table for deriving numerical age. J. Geol. 109, 155–170.
Mcarthur, J.M., Walsh, J.N., 1984. Rare-earth geochemistry of phosphorites. Chemical Geology 47, 191–220.
McCulloch, M., Wasserburg, G., 1978. Sm-Nd and Rb-Sr chronology of continental crust formation. Science 200, 1003–1011.
McLennan, S.M., 1989. RARE-EARTH ELEMENTS IN SEDIMENTARY-ROCKS - INFLUENCE OF PROVENANCE AND SEDIMENTARY PROCESSES. Rev. Mineral. 21, 169–200.
McLennan, S., Hemming, S., McDaniel, D., Hanson, G., 1993. Geochemical approaches to sedimentation, provenance, and tectonics. Geol. Soc. Am. Spec. Pap. 284, 21–40.
Melezhik, V., Pokrovsky, B., Fallick, A., Kuznetsov, A., Bujakaite, M., 2009. Constraints on 87Sr/86Sr of Late Ediacaran seawater: insight from Siberian high-Sr limestones. J. Geol. Soc. 166, 183–191.
Miller, J., Harris, N., 1989. Evolution of continental crust in the Central Andes; constraints from Nd isotope systematics. Geology 17, 615–617.
Nesbitt, H.W., Markovics, G., 1997. Weathering of granodioritic crust, long-term storage of elements in weathering profiles, and petrogenesis of siliciclastic sediments. Geochim. Cosmochim. Acta 61, 1653–1670.
Nesbitt, H., Young, G.M., 1982. Early Proteozoic climates and plate motions inferred from major element chemistry of lutites. Nature 299, 220.

Nesbitt, H.W., Young, G.M., 1984. Prediction of some weathering trends of plutonic and volcanic rocks based on thermodynamic and kinetic considerations. Geochim. Cosmochim. Acta 48, 1523–1534.
Nesbitt, H., Young, G.M., 1989. Formation and diagenesis of weathering profiles. J. Geol. 97, 129–147.
Nozaki, Y., Alibo, D.S., 2003. Importance of vertical geochemical processes in controlling the oceanic profiles of dissolved rare earth elements in the northeastern Indian Ocean. Earth & Planet Sci. Lett. 205, 155–172.
Nozaki, Y., Zhang, J., Amakawa, H., 1997. The fractionation between Y and Ho in the marine environment. Earth & Planet Sci. Lett. 148, 329–340.
O'nions, R., Hamilton, P., Hooker, P., 1983. A Nd isotope investigation of sediments related to crustal development in the British Isles. Earth & Planet Sci. Lett. 63, 229–240.
Panahi, A., Young, G.M., 1997. A geochemical investigation into the provenance of the Neoproterozoic Port Askaig Tillite, Dalradian Supergroup, western Scotland. Precambrian Res. 85, 81–96.
Peters, S.E., Gaines, R.R., 2012. Formation of the 'Great Unconformity' as a trigger for the Cambrian explosion. Nature 484, 363–366.
Pi, D.H., Liu, C.Q., Shields-Zhou, G.A., Jiang, S.Y., 2013. Trace and rare earth element geochemistry of black shale and kerogen in the early Cambrian Niutitang Formation in Guizhou province, South China: Constraints for redox environments and origin of metal enrichments. Precambrian Research 225, 218–229.
Picard, S., Lécuyer, C., Barrat, J.-A., Garcia, J.-P., Dromart, G., Sheppard, S.M., 2002. Rare earth element contents of Jurassic fish and reptile teeth and their potential relation to seawater composition (Anglo-Paris Basin, France and England). Chem. Geol. 186, 1–16.
Price, R.C., Gray, C.M., Wilson, R.E., Frey, F.A., Taylor, S.R., 1991. The effects of weathering on rare-earth element, Y and Ba abundances in Tertiary basalts from southeastern Australia. Chem. Geol. 93, 245–265.
Pufahl, P.K., Groat, L.A., 2017. Sedimentary and Igneous Phosphate Deposits: Formation and Exploration: An Invited Paper. Econ. Geol. 112, 483–516.
Reynard, B., Lécuyer, C., Grandjean, P., 1999. Crystal-chemical controls on rare-earth element concentrations in fossil biogenic apatites and implications for paleoenvironmental reconstructions. Chem. Geol. 155, 233–241.
Richter, F.M., Rowley, D.B., DePaolo, D.J., 1992. Sr isotope evolution of seawater: the role of tectonics. Earth & Planet Sci. Lett. 109, 11–23.
Sanematsu, K., Kon, Y., Imai, A., Watanabe, K., Watanabe, Y., 2013. Geochemical and mineralogical characteristics of ion-adsorption type REE mineralization in Phuket. Thailand. Miner. Depos. 48, 437–451.
Sawaki, Y., Ohno, T., Fukushi, Y., Komiya, T., Ishikawa, T., Hirata, T., Maruyama, S., 2008. Sr isotope excursion across the Precambrian-Cambrian boundary in the Three Gorges area. South China. Gondwana Res. 14, 134–147.
Shen, W., Ling, H., Li, W., Wang, D., 2000. Crust evolution in Southeast China: evidence from Nd model ages of granitoids. Sci. China Earth Sci. 43, 36–49.
Shi, C.H., 2005. Formation of phosphorite deposit, Breakup of Rodinia Supercontinent and Biology Explosion—A Case Study of Weng'an, Kaiyang and Zhijin Phosphorite Deposits of Guizhou Province. Ph.D. Thesis, Institute of Geochemistry Chinese Academy of Sciences (In Chinese with English abstract).
Shields, G., Stille, P., 2001. Diagenetic constraints on the use of cerium anomalies as palaeoseawater redox proxies: an isotopic and REE study of Cambrian phosphorites. Chem. Geol. 175, 29–48.
Shields, G.A., Webb, G.E., 2004. Has the REE composition of seawater changed over geological time? Chemical Geology 204, 103–107.
Shields-Zhou, G., Zhu, M., 2013. Biogeochemical changes across the Ediacaran-Cambrian transition in South China. Precambrian Research 225, 1–6.
Steiner, M., Li, G., Qian, Y., Zhu, M., Erdtmann, B.D., 2007. Neoproterozoic to early Cambrian small shelly fossil assemblages and a revised biostratigraphic correlation of the Yangtze Platform (China). Palaeogeography, Palaeoclimatology, Palaeoecology 254, 67–99.
Tosca, N.J., Johnston, D.T., Mushegian, A., Rothman, D.H., Summons, R.E., Knoll, A.H., 2010. Clay mineralogy, organic carbon burial, and redox evolution in Proterozoic oceans. Geochim. Cosmochim. Acta 74, 1579–1592.
Van De Flierdt, T., Pahnke, K., Amakawa, H., Andersson, P., Basak, C., Coles, B., Colin, C., Crocket, K., Frank, M., Frank, N., 2012. GEOTRACES intercalibration of neodymium isotopes and rare earth element concentrations in seawater and suspended particles. Part 1: reproducibility of results for the international intercomparison. Limnol. Oceanogr. Methods 10, 234–251.
Wang, J., Li, Z.-X., 2003. History of Neoproterozoic rift basins in South China: implications for Rodinia break-up. Precambrian Res. 122, 141–158.
Wang, Q., Wyman, D.A., Li, Z.-X., Bao, Z.-W., Zhao, Z.-H., Wang, Y.-X., Jian, P., Yang, Y.-H., Chen, L.-L., 2010. Petrology, geochronology and geochemistry of ca. 780Ma A-type granites in South China: Petrogenesis and implications for crustal growth during the breakup of the supercontinent Rodinia. Precambrian Research 178, 185–208.
Webb, G.E., Kamber, B.S., 2000. Rare earth elements in Holocene reefal microbialites: A new shallow seawater proxy. Geochim. Cosmochim. Acta 64, 1557–1565.
Wedepohl, K.H., 1995. The Composition of the Continental Crust. Geochim. Cosmochim. Acta 59, 1217–1232.
Wei, S., Fu, Y., Liang, H., Ge, Z., Zhou, W., Wang, G., 2017. Re–Os geochronology of the Cambrian stage-2 and -3 boundary in Zhijin County, Guizhou Province, China. Acta Geochimica 37, 323–333.
Wei, G.-Y., Ling, H.-F., Shields, G.A., Chen, T., Lechte, M., Chen, X., Qiu, C., Lei, H., Zhu, M., 2019. Long-term evolution of terrestrial inputs from the Ediacaran to early Cambrian: Clues from Nd isotopes in shallow-marine carbonates. South China. Palaeogeogr. Palaeoclimatol. Palaeoecol. 535, 109367.
Wood, S.A., 1990. The aqueous geochemistry of the rare-earth elements and yttrium: 1. Review of available low-temperature data for inorganic complexes and the inorganic REE speciation of natural waters. Chem. Geol. 82, 159–186.
Wronkiewicz, D.J., Condie, K.C., 1987. Geochemistry of Archean shales from the Witwatersrand Supergroup, South Africa: source-area weathering and provenance. Geochim. Cosmochim. Acta 51, 2401–2416.
Wu, S., Yang, H., Fan, H., Xia, Y., Meng, Q., He, S., Gong, X., 2022. Assessment of the Effect of Organic Matter on Rare Earth Elements and Yttrium Using the Zhijin Early Cambrian Phosphorite as an Example. Minerals 12, 876.
Xing, J., Jiang, Y., Xian, H., Zhang, Z., Yang, Y., Tan, W., Liang, X., Niu, H., He, H., Zhu, J., 2021. Hydrothermal activity during the formation of REY-rich phosphorites in the early Cambrian Gezhongwu Formation, Zhijin, South China: A micro-and nano-scale mineralogical study. Ore Geol. Rev. 136, 104224.
Xu, J., Xiao, J., Yang, H., Xia, Y., Wu, S., Xie, Z., 2019. The REE enrichment characteristics and constraints of the phophorite in Zhijin, Guizhou: A case study of No. 2204 drilling cores in the Motianchong ore block. Acta Mineral. Sin. 39, 371–379 in Chinese with English abstract.
Yang, H., Xiao, J., Xia, Y., Xie, Z., Tan, Q., Xu, J., He, S., Wu, S., Liu, X., Gong, X., 2021a. Phosphorite generative processes around the Precambrian-Cambrian boundary in South China: An integrated study of Mo and phosphate O isotopic compositions. Geosci. Front. 12, 101187.
Yang, H., Zhao, Z., Xia, Y., Xiao, J., 2021b. REY Enrichment Mechanisms in the early Cambrian Phosphorite from South China. Sediment Geol. 426, 106041.
Yin, R.S., Xu, L.G., Lehmann, B., Lepak, R.F., Hurley, J.P., Mao, J.W., Feng, X.B., Hu, R. Z., 2017. Anomalous mercury enrichment in Early Cambrian black shales of South China: Mercury isotopes indicate a seawater source. Chem. Geol. 467, 159–167.
Young, G.M., 2002. Geochemical investigation of a Neoproterozoic glacial unit: the Mineral Fork Formation in the Wasatch Range. Utah. Geol. Soc. Am. Bull. 114, 387–399.
Zhang, H., Fan, H., Wen, H., Han, T., Zhou, T., Xia, Y., 2022. Controls of REY enrichment in the early Cambrian phosphorites. Geochimica et Cosmochimica Acta 324, 117–139.
Zhang, Z., Jiang, Y., Niu, H., Xing, J., Yan, S., Li, A., Weng, Q., Zhao, X., 2021. Enrichment of rare earth elements in the early Cambrian Zhijin phosphorite deposit, SW China: Evidence from francolite micro-petrography and geochemistry. Ore Geol. Rev. 138, 104342.
Zhang, S.B., Zheng, Y.F., 2013. Formation and evolution of Precambrian continental lithosphere in South China. Gondwana Res. 23, 1241–1260.
Zhang, X.L., Zhou, X., Hu, D.P., 2020. High-resolution paired carbon isotopic records from the Meishucun section in South China: Implications for carbon cycling and environmental changes during the Ediacaran-Cambrian transition. Precambrian Res. 337, 105561.
Zhao, J., McCulloch, M., Bennett, V., 1992. Sm-Nd and U-Pb zircon isotopic constraints on the provenance of sediments from the Amadeus Basin, central Australia: Evidence for REE fractionation. Geochim. Cosmochim. Acta 56, 921–940.
Zhao, J.-H., Zhou, M.-F., Zheng, J.-P., 2013. Neoproterozoic high-K granites produced by melting of newly formed mafic crust in the Huangling region. South China. Precambrian Res. 233, 93–107.
Zhou, L., Zhang, Z., Li, Y., You, F., Wu, C., Zheng, C., 2013. Geological and geochemical characteristics in the paleo-weathering crust sedimentary type REE deposits, western Guizhou. China. J. Asian Earth Sci. 73, 184–198.
Zhu, Y., Lai, S., Qin, J., Zhu, R., Zhang, F., Zhang, Z., Zhao, S., 2019. Neoproterozoic peraluminous granites in the western margin of the Yangtze Block, South China: Implications for the reworking of mature continental crust. Precambrian Res. 333, 105443.
Zhu, Y., Lai, S.-C., Qin, J.-F., Zhu, R.-Z., Zhang, F.-Y., Zhang, Z.-Z., 2020. Petrogenesis and geochemical diversity of Late Mesoproterozoic S-type granites in the western Yangtze Block, South China: Co-entrainment of peritectic selective phases and accessory minerals. Lithos 352, 105326.
Zhu, R., Li, X., Hou, X., Pan, Y., Wang, F., Deng, C., He, H., 2009. SIMS U-Pb zircon age of a tuff layer in the Meishucun section, Yunnan, southwest China: Constraint on the age of the Precambrian-Cambrian boundary. Science in China Series D: Earth Sciences 52, 1385–1392.
Zhu, M., Zhang, J., Yang, A., Li, G., Steiner, M., Erdtmann, B.D., 2003. Sinian-Cambrian stratigraphic framework for shallow-to deep-water environments of the Yangtze Platform: an integrated approach. Prog. Nat. Sci. 13, 951–960.